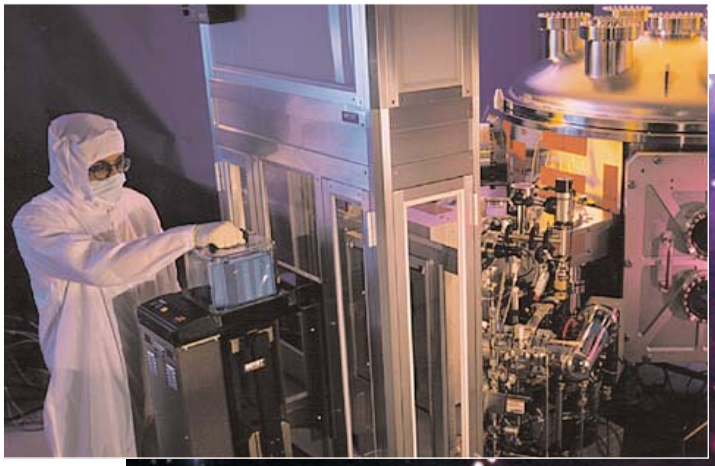

Optics in 2000

Guest Editor: Bob D. Guenther
Physics Department, Duke University

Examples of the most significant recent research in optics and engineering are published each year in the December issue of OPN. This issue is comprised of short descriptions of the "hottest" topics in current optics research. Selection criteria applied to submissions are as follows:

- **the accomplishments described must have been published in a refereed journal in the year prior to publication in OPN;**
- **the work must be illustrated in a clear, concise manner, comprehensible to the at-large optics community;**
- **the topical area as a whole must be described, and the importance of the research must be detailed.**

There are no requirements in the selection process for inclusion of specific topical areas. When a large number of submissions are received for a specific area, this is taken as evidence that the topic has been fertile ground for activity and research over the course of the preceding year. OPN strives to ensure that engineering, science, and technology are all represented. The number of papers accepted overall is limited by space.

With 33 papers accepted, 2000 has proven to be another successful year. OPN and OSA would like to thank the hundreds of researchers from all over the world who submitted summaries to Optics in 2000.

1047-6938/00/12/0016/32-$0015.00

Fiber Optic Communication

Fiber Bragg Gratings Enable Optical Code-Division Multiple Access

By Lawrence R. Chen and Peter W. E. Smith

Optical code-division multiple access (OCDMA) is a technique well suited for local area networks. Data from multiple users are encoded differentially, multiplexed on a single transmission medium, demultiplexed, and passed through code-specific detection. Discrimination of unwanted signals is achieved by means of assigning minimally interfering codes to each user. Attractive features of OCDMA include the ability to support asynchronous bursts of traffic; transparency to overlaid transport protocols such as SONET, IP, or ATM; the potential for increased security; and high capacity (through the interconnection of a large number of users operating at modest data rates). Enabling device technologies are required for encoding data at the transmitters and for providing code discrimination at the receivers. Recently there have been several proposals and demonstrations involving use of fiber Bragg gratings (FBGs) for encoding-decoding in a variety of OCDMA schemes, including those based on wavelength-encoding (WE), time-spreading (TS), and hybrid approaches.[1-5]

We have developed a hybrid WE-TS OCDMA system that uses chirped moiré fiber Bragg gratings (CMGs) for encoding-decoding.[6,7] The encoding process involves reflection of a broadband pulse (representing 1) from a CMG. The reflected (encoded) signal consists of wavelengths from the broadband input temporally separated in a specific order as defined by the combined spectral and temporal characteristics of the CMG. In the decoding process the wavelengths must be recovered in the same time slot (despread). Thus the encoder and the decoder consist of identical CMGs with encoding-decoding performed by bidirectional reflections (opposite ends) from the gratings.

User-specific codes are defined by the combined spectral and temporal characteristics of the CMGs. By tailoring the spectral response, many different user codes can be generated from one CMG structure. These codes are termed strictly orthogonal—which means that they have different WE and different TS patterns with no overlapping wavelengths—or quasi orthogonal—which means that they have different WE patterns but the same TS pattern and at most one overlapping wavelength. The code length N is determined by the total number of wavelengths available, which in turn is set by the bandwidth of the broadband source or the CMG characteristics. The code weight w is determined by the number of code bits (each at a different wavelength) in each code.

We have developed algorithms for generating codes (given the constraints imposed by the CMG structures) and have analyzed system performance in terms of the effects of multiuser interference on bit error rate (BER).[6] The results, illustrated in Figure 1, show the potential capabilities of our OCDMA system. In particular, for $N = 21$ and $w = 3$, 48 simultaneous users can operate with a BER of 10^{-9}. In practical terms this requires ≈11-cm-long grating structures, resulting in a maximum single-channel data rate of ≈940 Mbit/s or an aggregate data rate of 45 Gbit/s. We have also demonstrated a four-user OCDMA system.[7] Measurements at OC-12 transmission rates clearly show the rejection of multiuser interference and proper recovery of a desired user's bit sequence (see Figure 2).

Using CMGs to perform encoding-decoding all optically and all in-fiber results in a cost-effective OCDMA implementation that minimizes the amount of electronic processing and facilitates packaging of the encoder-decoder structures. We believe that FBGs will play increasingly crucial roles in the ongoing development of OCDMA systems.

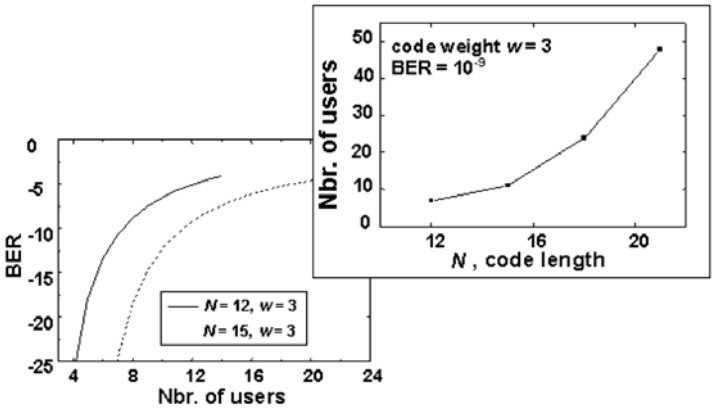

Fiber Bragg Gratings Figure 1. BER as a function of the number of simultaneous users for different N and w and the number of simultaneous users at a BER of 10^{-9} as a function of N for $w = 3$.

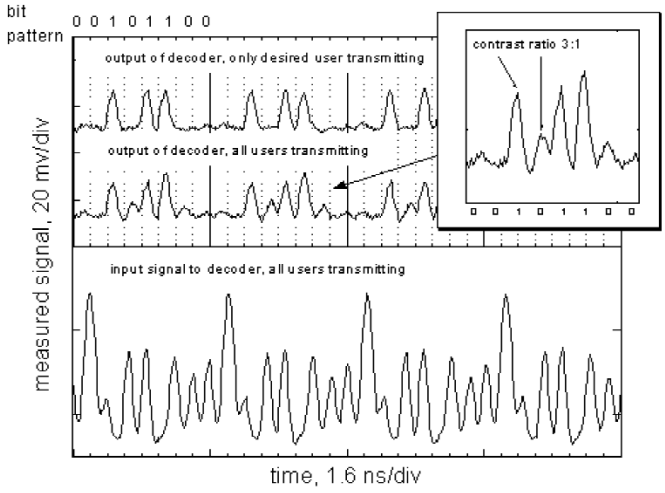

Fiber Bragg Gratings Figure 2. Experimental demonstration of encoding–decoding an 8-bit RZ pattern (0 0 1 0 1 1 0 0) in a four-user system (one desired and three interferers) at an OC-12 transmission rate (622.08 Mbit/s). The codes have $N = 7$ and $w = 3$. Of the three interferers, one has a quasi-orthogonal code and two have strictly orthogonal codes. The peak contrast ratio between properly and improperly decoded signals is 3:1 as defined by the code weights used (the interference is dominated by the user with the quasi-orthogonal code).

References

1. H. Fathallah, L. A. Rusch, and S. LaRochelle, "Passive optical fast frequency hop CDMA communication system," J. Lightwave Technol. **17**, 397-405 (1999).
2. D. B. Hunter and R. A. Minasian, "Programmable high-speed optical code recognition using fiber Bragg grating arrays," Electron. Lett. **35**, 412 (1999).
3. A. Grunnet-Jepsen, A. E. Johnson, E. S. Maniloff, T. W. Mossberg, M. J. Munroe, and J. N. Sweetser, "Fiber Bragg grating based spectral encoder/decoder for lightwave CDMA," Electron. Lett. **35**, 1096 (1999).
4. G. E. Town, K. Chan, and G. Yoffe, "Design and performance of high-speed optical pulse-code generators using optical fiber Bragg gratings," IEEE J. Sel. Top. Quantum Electron. **5**, 1325 (1999).
5. N. Wada, H. Sotobayashi, and K. Kitayama, "2.5 Gbit/s time-spread/wavelength-hop optical code division multiplexing using fiber Bragg grating with supercontinuum light source," Electron. Lett. **36**, 815 (2000).
6. L. R. Chen, P. W. E. Smith, and C. M. de Sterke, "Wavelength-encoding/temporal-spreading optical code-division multiple-access system with in-fiber chirped moiré gratings," Appl. Opt. **38**, 4500 (1999).
7. L. R. Chen and P. W. E. Smith, "Demonstration of incoherent wavelength-encoding/time-spreading optical CDMA using chirped moiré gratings" IEEE Photon. Technol. Lett. **12**, 1281 (2000).

Dense Wavelength Division Multiplexing in Parallel Sysplex and Storage Area Networks

By Casimer DeCusatis

Many data processing and storage systems consume multiterabyte aggregate bandwidth in metropolitan area networks. These datacom applications require high availability (99.999% or better), fault tolerance, and guaranteed quality of service for all communication protocols. In addition, enterprise servers or mainframes have adopted parallel processing architectures, such as Parallel Sysplex,[1] which uses fiber-optic links to interconnect microprocessors and distribute time-of-day clock signals with low jitter over distances as great as 40 km. These requirements, coupled with fiber exhaust in metropolitan areas, are driving the widespread use of dense optical wavelength division multiplexing (DWDM). The requirements of voice, video, data, and Internet protocol (IP) traffic were previously addressed by separate overlay networks; however, the rapid growth of Internet traffic and e-commerce has created interest in a service-transparent DWDM backbone capable of allocating bandwidth on demand. This offers the advantages of a highly scaleable, low-cost, protocol-independent infrastructure and may be the first step toward switchable, all-optical networks.

In this paper we describe a DWDM solution recently developed and tested for this environment, the IBM 2029 Fiber Saver.[2-4] Optical signal multiplexing is performed with passive thin-film interference filters; filter banks are cascaded in series to provide as many as 32 full duplex channels (wavelengths) multiplexed over a single pair of fibers with industry standard wavelengths.[5,6] Unidirectional protection switching at the physical layer is configurable on a per channel basis (with a maximum switching time of 50 ms) to restore service in the event of either a fiber break or hardware failure. This ensures that there are no single points of failure in a protected or high-availability channel. The multiplexer is also a complete 3R repeater (*retimes* the signal to remove jitter, *reshapes* the signal to remove pulse distortion, and *regenerates* the average optical power). This multiplexer supports native attachment of all industry standard protocols including ESCON, FICON, Fibre Channel, Asynchronous Transfer Mode (ATM), Fiber Distributed Data Interface (FDDI), Gigabit Ethernet, and Parallel Sysplex up to 1.25 Gbit/s/channel.

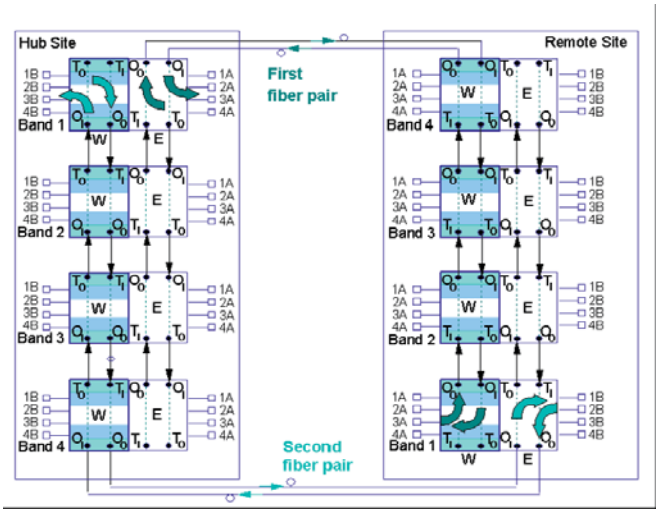

Dense Wavelength Division Multiplexing Figure 1. Cascade of optical filters in a Fiber Saver DWDM network. As many as eight shelves can be cascaded in a dual counter-rotating ring to form a 32:1 wavelength multiplexer; for simplicity the figure illustrates only four shelves at the hub and at remote locations in a point-to-point network. Each shelf is divided into an east and a west side, and individual channels are shown as 1A, 1B, and so on. The two fiber pairs in this example can be configured to carry 16 unprotected wavelengths each for a total of 32 independent channels, or the 16 wavelengths on the first fiber pair can be backed up or protected by the 16 wavelengths on the second fiber pair. Any combination of protected or unprotected channels is possible.

Cascaded filter banks are configured as dual self-healing counter-rotating fiber rings, as shown in Figure 1. This supports new topologies including fully protected point-to-point links and rings with as many as nine physical locations. The maximum distance for point-to-point links is 50 km/15 dB, whereas the maximum distance between any two nodes on a ring is 35 km/10.5 dB (additional MUX-DEMUX stages in ring topologies allow for passive add-drop of wavelengths). Each data channel includes a low-speed in-band service channel, which carries network management information. The entire network can thus be monitored from a single point over an IP connection; Java-enabled software provides a graphical user interface that supports standard network management applications such as SNMP.

We have built and tested a large datacom system with this multiplexer at the IBM TeraPlex Center.[2-4] A fully protected 32-wavelength DWDM network was used to configure two IBM G6 Enterprise Servers in a Parallel Sysplex. A combination of four ESCON and four FICON channels were routed through a 9032-5 ESCON Director equipped with a FICON Bridge feature and used to drive various storage area network devices, including a 3495 automated tape library and a Brocade switch fabric. One channel each of FDDI, ATM 155 over SONET (OC-3), and Gigabit Ethernet LX were run from the mainframe open system adapter interface

cards to an assortment of LAN connections, such as a Cisco Catalyst 5000 router. Spools of fiber were used to simulate intersite links with maximum distance and loss, including eight optical connectors in the link for deliberate introduction of connector return loss and modal noise. Various applications were used to simulate stressful network traffic, including LINUX, MVS, and UNIX operating systems, Lotus Domino databases, and transaction processing with high-security encryption (NIST Level 4 Certified cryptography). System code on the processors was used to log bit errors on all links as well as any other conditions indicating either failure or degraded performance. All fiber-optic links operated error free (extrapolated to 10^{-15} bit error rate) over a 72-h test run and over a 3-week extended performance test that included opening individual fiber sections in a high-availability configuration; pulling and reseating cards with the system powered on; and causing failure to power supplies, cooling fans, and other components to verify that there were no single points of failure. Future directions for this research may include development of subrate time-division multiplexing and intelligent bandwidth management techniques such as digital wrapper encapsulation.

References and Note

1. The names Parallel Sysplex, ESCON, FICON, 2029 Fiber Saver, 9032-5, 3495, and G6 Enterprise Server are registered trademarks of IBM Corporation. The name Domino is a registered trademark of Lotus Corporation. The name Catalyst 5000 is a registered trademark of Cisco Systems Corporation.
2. C. DeCusatis, "Optoelectronics for multi-terabit intelligent wavelength division multiplexing networks," in *Proceedings of the IEEE Summer Topical Meeting on Electronic Enhanced Optics* (Institute of Electrical and Electronics Engineers, New York, 2000), pp. 41-2.
3. C. DeCusatis and D. Priest, "Dense wavelength division multiplexing devices for metropolitan area datacom and telecom networks," in *Proceedings of the International Conference on Applications of Photonics Technology (Photonics North),* IEEE, Montreal, Quebec, Canada, 2000, pp. 8-9; "Multiplexer increases traffic capabilities," Research and Development Magazine, **42** (9), p. 119, September 2000.
4. C. DeCusatis and P. Das, "Subrate multiplexing using time and code division multiple access in dense wavelength division multiplexing networks," in *Proceedings of SPIE Workshop on Optical Networks* (Society of Photo-Optical Instrumentation Engineers, Bellingham, Wash., 2000), pp. 3-11.
5. C. DeCusatis, E. Maass, D. Clement, and R. Lasky, eds., *Handbook of Fiber Optic Data Communication* (Academic, New York, 1998).
6. "Optical interface for multichannel systems with optical amplifiers," draft standard G.MCS, annex A4 of standard COM15-R-67-E (available from the International Telecommuncation Union, Geneva, 1999).

Fax Today! See page 63.

INTERFEROMETRY

Dense Plasma Diagnostics with an Amplitude-Division Soft-X-Ray Laser Interferometer Based on Diffraction Gratings

By Jorge Filevich, Kelly Kanizay, Mario C. Marconi, Juan L. A. Chilla, and Jorge J. Rocca

Interferometry with optical lasers has been used for decades to obtain multidimensional maps of the electron density in a large variety of dense plasmas. However, free-free absorption and refraction of the probe beam limit the maximum electron density, plasma size, and plasma density gradient that can be probed. Laboratory soft-x-ray lasers have been used to extend the limits of plasma interferometry.[1] The recent development of gain-saturated tabletop soft-x-ray lasers[2] has created the opportunity for developing portable soft-x-ray tools that will allow for detailed maps of the electron density evolution in a great variety of dense plasmas. With this aim we have developed what we believe is a novel soft-x-ray amplitude-division interferometer in which diffraction gratings are used as beam splitters.[3] By proper tailoring of the gratings, the interferometer can be made to operate at any selected soft-x-ray wavelength. An additional advantage of using diffraction gratings is their increased resistance to catastrophic damage produced by fast particle debris.

The soft-x-ray interferometer, which consists of a modified Mach-Zehnder configuration, is schematically illustrated in Figure 1 (top). The soft-x-ray laser beam is diffracted off the first grating into the two arms of the interferometer. The incidence angle and blaze of the grating are selected to allow most of the laser radiation to be evenly split between the zero and the first diffraction orders. Two elongated grazing incidence mirrors are placed on the zero- and the first-order arms to redirect the light toward the second grating, which recombines the beams to generate the interference pattern. The plasma to be studied is introduced in one of the arms of the interferometer and is imaged with a magnification of 25X onto a microchannel-plate CCD detector. The interferometer was used in combination with a 46.9-nm capillary discharge tabletop laser to map the electron density evolution of a line-focused laser-created plasma generated onto a Cu slab target. The plasma was generated by means of focusing a 360-mJ Q-switched Nd:YAG laser (λ = 1.06 μm) into a ~30-μm-wide line focus ~2.7 mm in length.

Figure 1 (bottom) shows a sequence of interferograms that describe the evolution of the laser-created plasma. Electron density maps were computed from the measured number of fringe shifts at each location. We have been able to probe the plasma at locations as close as 25-30 μm from the target, where the electron density is ≈5 x 10^{19} cm^{-3} and the density gradient is steep.

Another series of measurements for 1.8-mm-long line-focus plasmas created by 0.6-J Nd:YAG laser pulses probed electron densities as great as 1 x 10^{20} cm^{-3}. Ray-

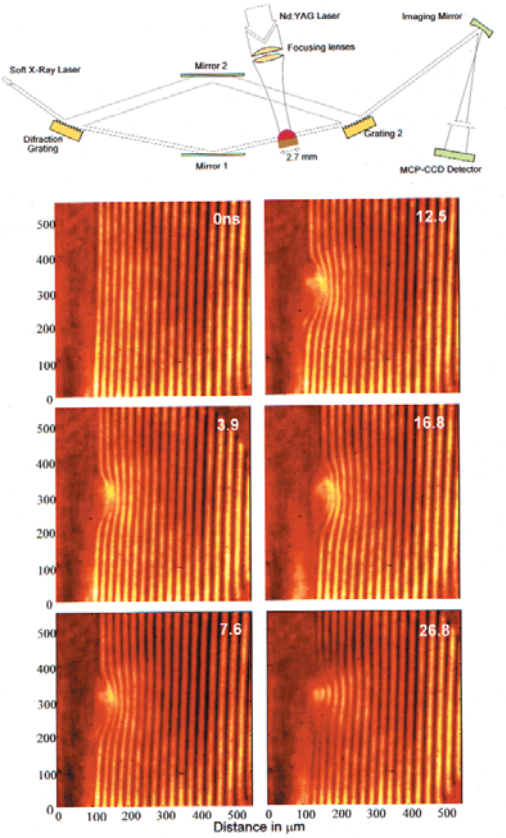

Dense Plasma Diagnostics Figure 1. (Top) Schematic diagram of the soft x-ray amplitude-division grating interferometer and plasma diagnostics set up. (Bottom) Sequence of soft x-ray interferograms depicting the evolution of a 2.7mm long line-focus plasma generated by a Q-Switched Nd:YAG laser.

tracing computations show that these measurements would be difficult to realize with an ultraviolet laser, owing to strong refraction caused by the large density gradients.

In conclusion, we have demonstrated what to our knowledge is a new soft-x-ray interferometer that can be combined with any of the currently available saturated soft-x-ray lasers to study many high-density laboratory plasmas of significant current interest. The use of this interferometer with shorter-wavelength soft-x-ray lasers of short pulse duration will allow for the probing of near-solid-density plasmas.

This research was funded by the U.S. Department of Energy. The laser was developed with the support of the National Science Foundation. We acknowledge a grant from the W. M. Keck Foundation.

References

1. L. B. Da Silva, T. W. Barbee, Jr., R. Cauble, P. Celliers, D. Ciarlo, S. Libby, R. A. London, D. Matthews, S. Mrowka, J. C. Moreno, D. Ress, J. E. Trebes, A. S. Wan, and F. Weber, "Electron density measurements of high density plasmas using soft-x-ray laser interferometry," Phys. Rev. Lett. **74**, 3991-4 (1995).
2. J. J. Rocca, "Table top soft x-ray lasers," Rev. Sci. Instrum. **70**, 3799-827, (1999).
3. J. Filevich, K. Kanizay, M. C. Marconi, J. L. A. Chilla, and J. J. Rocca, "Dense plasma diagnostics with an amplitude-division soft-x-ray laser interferometer based on diffraction gratings," Opt. Lett. **25**, 356-8 (2000).
4. B. R. Benware, C. D. Macchietto, C. H. Moreno, and J. J. Rocca, "Demonstration of a high average power table-top soft x-ray laser," Phys. Rev. Lett. **81**, 5804-7 (1998).

Interference Imaging For Aspheric Surface Testing

By Paul E. Murphy, Thomas G. Brown, and Duncan T. Moore

Aspheric optical surfaces provide superior performance in the design of optical systems. Yet their broad application requires effective design, fabrication, and metrology. Powerful computers and algorithms allow use of aspheres in lens design software. Modern computer-controlled fabrication processes automatically generate aspheres, and deterministic polishing processes, such as magnetorheological finishing (MRF), finish the part.[1] The lack of flexible metrology, however, remains a major bottleneck to many cost-effective solutions. Null interferometry is an accurate tool for the testing of spherical surfaces. Extending this capability to aspheres, however, requires the design and fabrication of special null optics.

Testing aspheres in a null configuration is both inflexible and expensive, thereby limiting their use in practical system designs. The ability to measure an asphere without corrective optics would alleviate this problem. Such non-null tests, however, have intrinsic barriers to implementation. Two effects in particular stifle non-null interferometry: the density of the interference fringes and the failure of the common-path assumption. Of these two problems, the common-path failure is more pervasive, leading to retrace errors that introduce bias into the measurement. Empirical techniques demonstrate some capability of predicting (and thus removing) such errors but do not indicate whether another interferometer design might perform better.[2,3]

A more fundamental model gives insight into the effects that drive the interference imaging errors. Huang analytically postulated the effects of some aberrations in a Fizeau interferometer and illustrated distortion experimentally.[4] We explore the effect of coherent fringe imaging in detail under a geometrical-optics framework.[5] One key contribution is a general expression for interference imaging errors as a function of the imaging system's conventional parameters. The errors are subclassified into phase and mapping and are predicted from the wavefront aberration of the imaging system. Figures 1(a) and 1(b) illustrate the concept of phase and mapping errors. Our method predicts these errors from the imaging system parameters and the slope departure of the test wavefront (from the reference). Analytic results are obtained through aberration theory, presenting a powerful framework for describing non-null interference. Experiments on tilted and defocused spheres by use of a single-element imager demonstrated agreement with the theory to better than tenth-wave on some forty waves of defocus.[6]

General prediction of interferometer errors has several important applications. The amount of measurement error can be quickly estimated. Better still, the errors can be removed, although uncertainties in the imaging aberration values limit such a correction. Unknown tilt and decentration of the individual imaging elements introduce systematic errors in the aberrations, although even this problem can potentially be addressed with system calibration. Another application of the analysis is in the design of interferometers. Conventional analysis methods typically apply only to a particular interferometer, and thus comparison between designs is quite tedious. The methods presented in this research are based on the conventional aberration characteristics of the interferometer imaging system. Inasmuch as the imaging error predictions are general, they can be optimized. The manifold tools of lens design become available to non-null interferometer design, rather than relying on ad hoc methods.

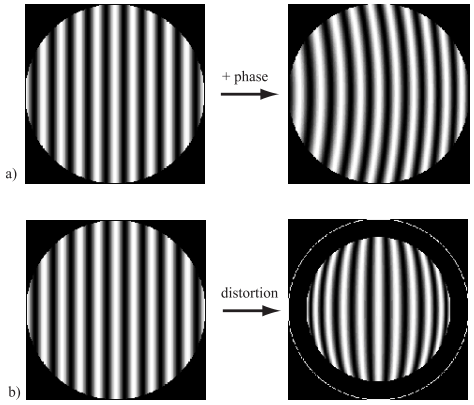

Interference Imaging Figure 1. Pictorial examples of phase and mapping errors. a) A phase error with quadratic dependence on part position. b) The mapping error induced by 20% third-order barrel distortion.

References

1. D. Golini, S. D. Jacobs, V. W. Kordonski, and P. Dumas, "Precision optics fabrication using magnetorheological finishing," in Advanced Materials for Optics and Precision Structures, M. A. Ealey, R. A. Paquin, and T. B. Parsonage, eds., **Vol. CR67** of SPIE Critical Review Series (SPIE Press, Bellingham, Washington, 1997), pp. 251-74.
2. J. E. Greivenkamp, A. E. Lowman, and R. J. Palum, "Sub-Nyquist interferometry: implementation and measurement capability," Opt. Eng. **35**, 2962-9 (1996).
3. C. J. Evans, "Compensation for errors introduced by non-zero fringe densities in phase-measuring interferometers," CIRP Ann. Int. Inst. Prod. Eng. Res. **42/1**, 577-80 (1993).
4. C. Huang, "Propagation errors in precision Fizeau interferometry," Appl. Opt. **32**, 7016-21 (1993).
5. P. E. Murphy, T. G. Brown, and D. T. Moore, "Interference imaging for aspheric surface testing," Appl. Opt. **39**, 2122-9 (2000).
6. P. E. Murphy, T. G. Brown, and D. T. Moore, "Measurement and calibration of interferometric imaging aberrations," Appl. Opt. **39**, to be published, December 1, 2000.

LASERS

Single-Transverse-Mode Operation of a Coiled Multimode Fiber Amplifier

By Jeffrey P. Koplow, Dahv A. V. Kliner, and Lew Goldberg

Single-mode (SM), rare-earth-doped fiber lasers and amplifiers are widely used in telecommunications and other applications requiring compact, rugged optical sources with diffraction-limited beam quality. For appli-

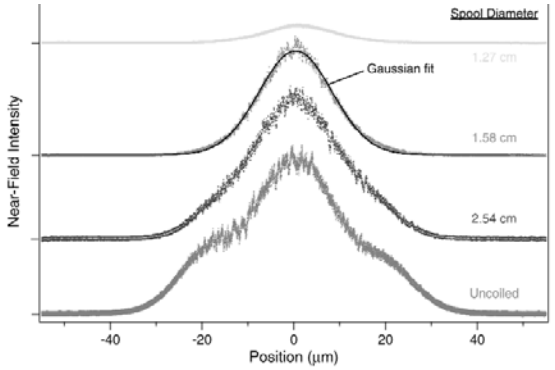

Multimode Fiber Amplifier Figure 1. Near-field intensity distribution of ASE from MM amplifier for the indicated spool diameters.

cations requiring high-peak-power pulses or narrow linewidth, however, use of fiber-based systems has been limited by the relatively low energy-storage capacity of SM fibers and by the onset of nonlinear processes in the fiber. These problems can be mitigated by increasing the core diameter of the fiber, but eventually the fiber will support higher-order modes; such multimode (MM) fibers are generally characterized by poor beam quality, which restricts their use in applications such as nonlinear frequency conversion, pumping of optical parametric oscillators and amplifiers, lidar, and materials processing.

Two approaches to overcoming these limitations have been reported. Taverner *et al.* developed erbium-doped fibers with low numerical apertures, which allowed the core size to be increased while maintaining SM operation.[1] Alternatively, several groups using MM fiber amplifiers have obtained varying levels of suppression of high-order modes by adjusting the launch conditions of the seed beam[2] or the fiber refractive-index and rare-earth-dopant distributions.[3]

In a recent paper,[4] researchers at the Naval Research Laboratory and Sandia National Laboratories reported a new approach to obtaining SM operation of a laser or amplifier employing MM fiber. This technique exploits the fact that the fundamental mode (LP_{01}) is least sensitive to bend loss when the fiber is coiled. Thus, by wrapping a gain fiber around a cylindrical mandrel whose radius is chosen to provide low loss for LP_{01} and high loss for higher-order modes, bend loss can be used as a form of distributed spatial filtering to suppress all but the fundamental mode of a MM fiber amplifier.

The technique was demonstrated by construction of an ytterbium-doped fiber amplifier using MM fiber with a core diameter of 25 μm (more than three times the diameter of a comparable SM fiber). The fiber was end pumped with 3.9 W at 975 nm, and the copropagating amplified-spontaneous-emission (ASE) power and near-field spatial profile (intensity versus position at the fiber output face) were measured to determine the optimum spool diameter (ASE uniformly excites all modes of the MM fiber). Figure 1 shows the near-field spatial profile for several spool diameters and demonstrates the suppression of higher-order modes before the onset of significant loss for LP_{01} (whose spatial profile is nearly Gaussian). Measurements with a 1.58-cm spool diameter demonstrated a rigorously diffraction-limited output beam and, when the amplifier was seeded at 1064 nm, a slope efficiency that was nearly unchanged from that of an uncoiled amplifier. A maximum output power of 4.1 W was obtained with 11 W of pump power.

This new approach does not increase system complexity, is inexpensive to implement, and is compatible with (and may be extended by) other methods for suppressing modes above LP_{01}. It will allow for scaling of pulsed fiber lasers and amplifiers to significantly higher pulse energies and peak powers and cw fiber sources to higher average powers while maintaining excellent beam quality.

References

1. D. Taverner, D. J. Richardson, L. Dong, J. E. Caplen, K. Williams, and R. V. Penty, "158-μJ pulses from a single-transverse-mode, large-mode-area erbium-doped fiber amplifier," Opt. Lett. **22**, 378-80 (1997).
2. O. G. Okhotnikov and J. M. Sousa, "Flared single-transverse-mode fibre amplifier," Electron. Lett. **35**, 1011-13 (1999); M. Hofer, M. E. Fermann, A. Galvanauskas, D. Harter, and R. S. Windeler, "Low-noise amplification of high-power pulses in multimode fibers," IEEE Photonics Technol. Lett. **11**, 650-2 (1999).
3. H. L. Offerhaus, N. G. Broderick, D. J. Richardson, R. Sammut, J. Caplen, and L. Dong, "High-energy single-transverse-mode Q-switched fiber laser based on a multimode large-mode-area erbium-doped fiber," Opt. Lett. **23**, 1683-5 (1998).
4. J. P. Koplow, D. A. V. Kliner, and L. Goldberg, "Single-mode operation of a coiled multimode fiber amplifier," Opt. Lett. **25**, 442-4 (2000).

Gain Switching and Active Mode Locking Of Mid-Infrared Quantum Cascade Lasers

By Roberto Paiella, Federico Capasso, Claire Gmachl, Clyde G. Bethea, Harold Y. Hwang, Deborah L. Sivco, James N. Baillargeon, Albert L. Hutchinson, Alfred Y. Cho, and H. C. Liu

Quantum cascade (QC) lasers[1] are light sources based on optical transitions between quantized states of the conduction band in semiconductor nanostructures. These devices emit in the mid-infrared spectral region, which is known as the molecular fingerprint region, because many chemical and biological species have their telltale absorption features at these wavelengths. This spectral range is characterized by the lack of convenient laser sources of ultrashort pulses. On the other hand, these sources would be quite desirable for several applications, ranging from time-resolved spectroscopy to coherent control. Recently, we demonstrated the generation of picosecond mid-infrared pulses with gain-switched and actively mode-locked QC lasers.

Gain switching consists of driving an injection laser, biased below threshold, with short electrical pulses to generate even shorter optical pulses. In particular, we used a commercial step-recovery diode (comb generator) that produced voltage pulses of approximately 90 ps at a repetition rate of 100 MHz to gain switch several QC lasers, properly packaged for high-speed operation.[2] A typical output pulse from an 8-μm device is shown in the left-hand panel of the figure, as measured with a high-speed quantum-well infrared photodetector (QWIP).[3] A pulse duration of 89 ps is directly obtained from this trace; accounting for the finite response time

of the detection electronics, this corresponds to an estimated actual optical pulse width of approximately 45 ps.

In the case of active mode locking, several longitudinal modes of the laser cavity are locked in phase by an external gain modulation at the cavity round-trip frequency f_{rt} to produce a train of pulses with a repetition rate also equal to f_{rt}. In this experiment[4] we used a relatively long (3.75-mm) 8-μm device, with a round-trip frequency of approximately 11.65 GHz. To obtain efficient laser modulation at this frequency, a new QC laser processing was developed, employing a thick (and hence low-parasitic-capacitance) layer of a chalcogenide glass ($Ge_{0.25}Se_{0.75}$) as the current blocking layer between the top metal contact and the active material. Evidence of successful mode locking is shown in the right-hand panel of the figure: in particular, as the laser is driven at a frequency that is closer and closer to f_{rt}, more and more longitudinal modes are driven above threshold by the modulation sidebands of their neighbors, as expected with active mode locking. The phase-locked nature of this multimode output was confirmed by the observation of a narrow spike centered at f_{rt} in the rf spectrum of the QWIP photocurrent. A detailed analysis of the optical spectra gives evidence of a large chirp for the resulting optical pulses because of self-phase modulation, and allows us to obtain an approximate estimate of 5 ps for their temporal width.

Although the results presented here were obtained with lasers held at liquid-helium temperature, gain switching and active mode locking were demonstrated up to temperatures greater than 100 K.[2,4] Furthermore, these techniques are applicable to QC lasers that emit at essentially any wavelength in the mid-infrared.

Acknowledgments

This study was partly supported by the Defense Advanced Research Projects Agency, U.S. Army Research Office, under contracts DAAG55-98-C-0050 and DAAD19-00-C-0096.

Gain Switching Figure 1. Left, oscilloscope trace of a gain-switched pulse from an 8-μm QC laser at 10 K. The laser is biased with a dc current of 200 mA, approximately 80% of its cw threshold. Right, optical spectra of the output of an actively mode-locked 8-μm QC laser at constant dc bias (900 mA, approximately 11% above the cw threshold) and temperature (10 K), for different values of the rf drive frequency.

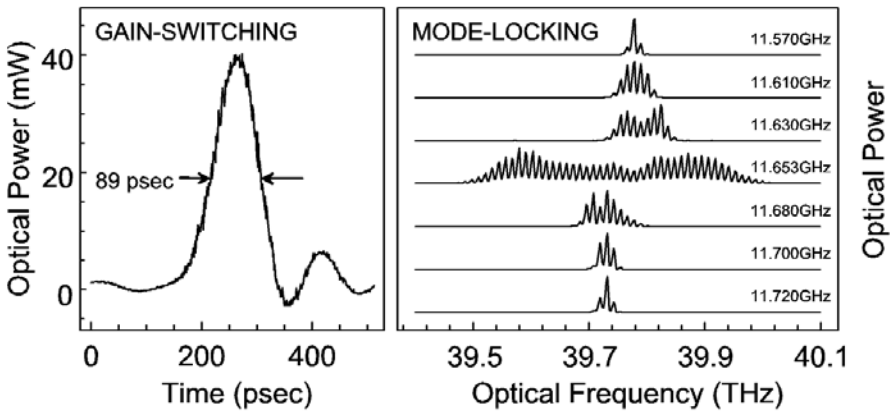

References

1. F. Capasso, C. Gmachl, A. Tredicucci, A. L. Hutchinson, D. L. Sivco, and A. Y. Cho, "High-performance quantum cascade lasers," Opt. Photon. News **10**, 31-7 (1999).
2. R. Paiella, F. Capasso, C. Gmachl, C. G. Bethea, D. L. Sivco, J. N. Baillargeon, A. L. Hutchinson, A. Y. Cho, and H. C. Liu, "Generation and detection of high-speed pulses of mid-infrared radiation with intersubband semiconductor lasers and detectors," IEEE Photon. Technol. Lett. **12**. 780-2 (2000).
3. H. C. Liu, J. Li, M. Buchanan, and Z. R. Wasilewski, "High-frequency quantum-well infrared photodetectors measured by microwave-rectification technique," IEEE J. Quantum Electron. **32**, 1024-8 (1996).
4. R. Paiella, F. Capasso, C. Gmachl, H. Y. Hwang, D. L. Sivco, A. L. Hutchinson, A. Y. Cho, and H. C. Liu, "Monolithic active mode-locking of quantum cascade lasers," Appl. Phys. Lett. **77**, 169-77 (2000).

NONLINEAR OPTICS

Sub-Optical-Cycle Coherent Control In Nonlinear Optics

By Randy Bartels, Sterling Backus, Gleb Vdovin, Ivan P. Christov, Margaret M. Murnane, and Henry C. Kapteyn

Perhaps the most extreme example of nonlinear optics is the process of high-harmonic generation (HHG), in which coherent soft X-rays are emitted by atoms in the process of being ionized by an intense laser. In a recent study published in *Nature*,[1] we demonstrated that concepts of coherent control can be applied to HHG. This study is one of the first instances of the useful application of coherent control of quantum systems, and it demonstrates a new type of intra-atomic phase matching that highlights fundamental differences between HHG and other nonlinear processes.

X-rays are emitted in HHG as the result of a recollision process. The electron released from a field-ionized atom will oscillate in the electromagnetic field of the laser. This electron can reencounter its parent ion and recombine with it, releasing its kinetic energy as an X-ray photon. These recollision events result in a burst of X-rays every half-cycle of the driving laser field (every 1.2 fs for an 800-nm driving laser). The spectral and temporal characteristics of this emitted light depend on the quantum phase of the electron's wave function at the time of recollision.

The overall spectrum of the X-rays depends on constructive and destructive interference between these periodic X-ray bursts. By precisely sculpting the temporal shape of the driving laser pulse (which is only ~6 optical cycles in duration), we can control the interference between these X-ray bursts. This allows us to optimize the X-ray emission spectrum in a useful way, demonstrating a fundamentally new type of intra-atomic phase-matching process. This pulse reshaping results in

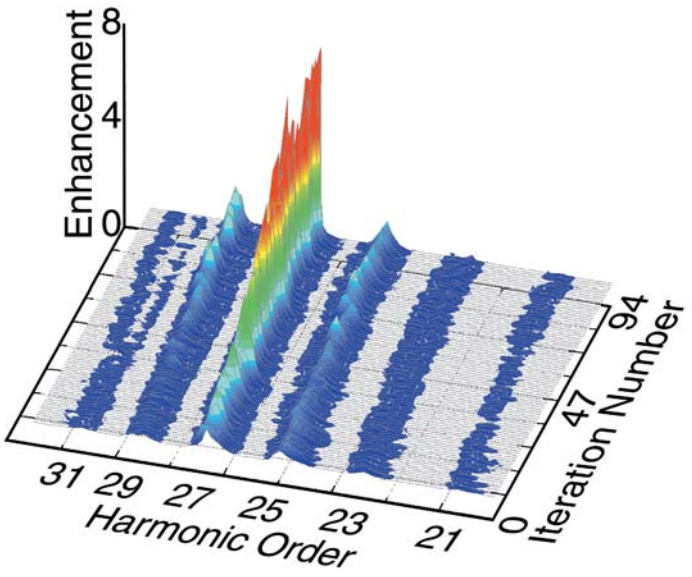

Sub-Optical-Cycle Coherent Control Figure 1. Optimization of a single (27th) harmonic in argon during suppression of adjacent harmonics. Reprinted from Reference 1, p. 164.

timing adjustments *within the laser pulse* that correspond to coherent control of the wave function on the 10-*attosecond* time scale.

To find the optimum pulse shape, we use a pulse-shaping apparatus in conjunction with an evolutionary, survival-of-the-fittest computer algorithm. The shape of an ultrashort pulse can be altered by means of changing the relative arrival times of the component colors of the pulse. By means of dispersing the pulse spectrum with a diffraction grating, then reflecting the dispersed light from a deformable mirror, local distortions of the mirror alter the arrival time of various component colors. Fig. 1 shows the result of optimization of the intensity of the 27th harmonic order, as the computer tries various pulse shapes, retaining the ones that generate the brightest X-rays. We see that the intensity of the 27th harmonic can be increased by 1 *order of magnitude* over that which was obtained with a transform-limited (18-fs) pulse. Furthermore, the brightness of other harmonic orders does not increase nearly as much, and the bandwidth of the 27th harmonic narrows. The optimized pulse shape results in electron recollisions that are now precisely in-phase for generating the 27th harmonic efficiently.

This result shows that, although most nonlinear processes are most efficient when driven with the highest possible peak-power—i.e., a transform-limited pulse—*high*-harmonic emission is optimized with a non-transform-limited pulse. This is because HHG is a fundamentally nonperturbative process. Slight changes in pulse shape can *channel* excitation from one high-order nonlinear process to another.

Reference

1. R. Bartels, S. Backus, E. Zeek, L. Misoguti, G. Vdovin, I. P. Christov, M. M. Murnane, and H. C. Kapteyn, "Shaped-pulse optimisation of coherent soft-x-rays," Nature **406**, 164-6 (2000).

Second-Order Nonlinear Optics Based on Chiral Materials

By Martti Kauranen, Bertrand Busson, Sven Van Elshocht, Thierry Verbiest, André Persoons, Colin Nuckolls and Thomas J. Katz

Second-order nonlinear optics has important applications in electro-optic modulation and frequency conversion of light. For efficient frequency conversion a material must fulfill two requirements. First, it must be noncentrosymmetric in order to produce a second-order response. Second, it must allow for phase matching so that the nonlinear source polarization and the generated field propagate through it in phase.

Macroscopic noncentrosymmetry is commonly achieved by use of materials with polar order. In the field of molecular nonlinear optics, polar order is usually brought about by alignment of molecular dipoles in an external field or by techniques that align molecules on surfaces. Such materials are often unstable, and their nonlinearity decreases with time. Phase matching is difficult to achieve, because the refractive indices of materials vary with wavelength. Consequently, the source polarization and the generated field propagate at different speeds. After a distance known as coherence length, they are 180° out of phase, and the intensity of the generated field starts to decrease. In quasi phase matching, the phase relation is restored by means of reversing the sign of the nonlinearity after every coherence length. This allows the field to grow quasi continuously. In polar materials quasi phase matching is achieved by periodic reversal of the polar axis direction.

We have shown that both high second-order nonlinearity[1] and quasi phase matching[2] can be achieved without polar order by use of chiral materials. Chiral molecules have no reflection symmetry and occur as two mirror-image forms (enantiomers). Enantiomerically

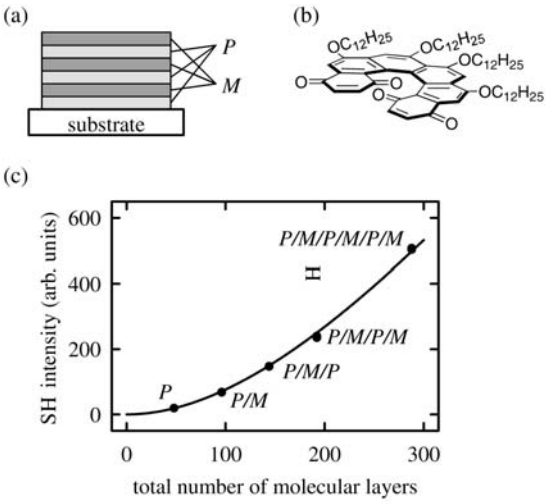

Second Order Nonlinear Optics Figure 1. (a) Alternating structures of the enantiomers (P and M) used to demonstrate quasi phase matching, (b) structure of the chiral helicenebisquinone, (c) continuous growth of the second-harmonic (SH) signal as a function of the number of molecular layers in quasi-phase-matched structures.

pure chiral materials are inherently noncentrosymmetric. They therefore give rise to a second-order response even when they have no polar order. In addition, the nonlinear coefficients associated with chirality are opposite in sign for the enantiomers, which allows for quasi phase matching in periodically alternating stacks of enantiomers [Figure 1(a)].

These phenomena were demonstrated by second-harmonic generation of a 1064-nm laser beam in Langmuir-Blodgett films of an enantiomerically pure aggregated helicenebisquinone [Figure 1(b)]. The response is dominated by nonlinear coefficients associated with chirality.[1] These coefficients are as great as >50 pm/V, which is sufficiently large for applications in photonic devices. The coherence length of the interaction was determined by recording of phase-matching curves with samples of varying thickness. For quasi phase matching,[2] each stack of enantiomers was set to be one coherence length thick, and the second-harmonic signal was demonstrated to grow continuously as a function of the number of stacks [Figure 1(c)].

The experiments show that both high second-order response and quasi phase matching can be achieved through the chirality of a material rather than through its polar order. Contrary to common belief, polar order is therefore not a fundamental requirement for efficient frequency-converting materials. Circumventing this requirement could lead to molecular nonlinear devices with increased stability. The principles are not limited to the layer-by-layer deposition of molecules that were used in these experiments. It is even possible that alternating structures of enantiomers could in the future be prepared by optical interconversion of enantiomers.[3] Chirality could therefore lead to completely new types of frequency converters with improved characteristics.

References

1. T. Verbiest, S. Van Elshocht, M. Kauranen, L. Hellemans, J. Snauwaert, C. Nuckolls, T. J. Katz, and A. Persoons, "Strong enhancement of nonlinear optical properties through supramolecular chirality," Science **282**, 913-5 (1998).
2. B. Busson, M. Kauranen, C. Nuckolls, T. J. Katz, and A. Persoons, "Quasi-phase matching in chiral materials," Phys. Rev. Lett. **84**, 79-82 (2000).
3. N. P. M. Huck, W. F. Jager, B. de Lange, and B. L. Feringa, "Dynamic control and amplification of molecular chirality by circular polarized light," Science **273**, 1686-8 (1996).

Determination of Acid-Base Equilibrium Constant of Organic Molecules and Biomolecules with 3rd-Order Nonlinear Optics

By Anderson S. L. Gomes, Cid B. de Araújo, Renato E. de Araujo, Arandi G. Bezerra, Jr., and Iouri E. Borissevitch.

Nonlinear optics has provided countless techniques and methods for characterization of materials.[1] We do not need to emphasize that the applications of nonlinear optics extend beyond physics, to chemistry, biology, and medicine. In particular, nonlinear optical properties of organic molecules and biomolecules have been extensively studied with the aim of achieving a basic understanding of them as well as photonic applications. In nature many biologically important molecules are acids or bases. A protonation reaction such as $H^+ + M \leftrightarrow MH^+$, involving a molecule M, is determined by an equilibrium constant K (sometimes K_a or K_b is used). In general K is affected by the molecular environment, which may also change the molecular structure. A simple mathematical description of the equilibrium constant K is given in terms of $pK = [(\log(K)]$, pH and molar concentration of the involved species by the Henderson-Hasselbalch equation, found in basic organic chemistry textbooks. The concentrations of two different species of a compound are the same when the pH of a medium is equal to the pK of the molecule in the solution.

Two methods are available to infer pK: linear optical absorption and electron paramagnetic resonance (EPR) if paramagnetic atoms are present. The first use of nonlinear optics for measurements of pK was reported by Xiao *et al.*,[2] exploring the technique of second-harmonic generation.

We introduced the use of third-order nonlinear optics to characterize pK in solutions as an elegant and reliable alternative by exploiting the well-known Z-scan technique.[3] The measurements were performed in a

Determination of Acid-Base Equilibrium Figure 1. (a) Results of nonlinear transmittance ΔT from Z-scan experiments (at room temperature) and EPR measurements at 4 Kelvin for Fe(III)TMPyP. Both techniques lead to the same pK value. (b) Transmission changes for the methyl orange solution that are due to nonlinear refraction (circles) and nonlinear absorption (inverted triangles).

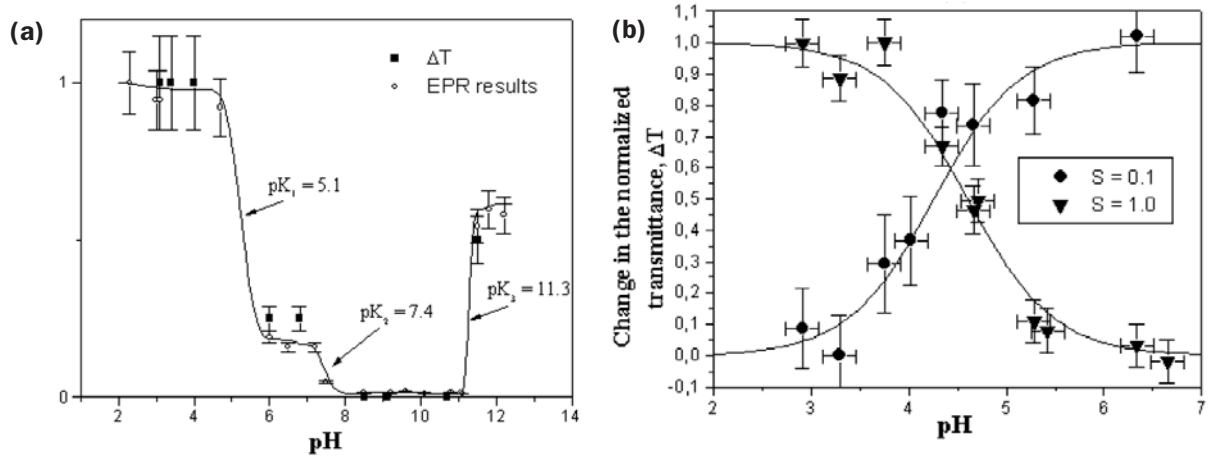

metalloporphyrin derivative,[4] which is an important biomolecule, as well as in a well-known pH indicator, methyl orange.[5] As with the *Z*-scan one can obtain either the nonlinear refraction or nonlinear absorption; we demonstrated that either of the two effects can be used to infer the pK of the material. Figure 1(a) shows the results for a porphyrin derivative, Fe(III)TmPyP in aqueous solution, where only the nonlinear refractive index was measured. Also shown are the EPR data obtained at 4 Kelvin. The curve is a guide to the eye. Figure 1(b) shows the data for methyl orange, whereby both nonlinear refraction and nonlinear absorption were measured. The values obtained for pK in both cases are in good agreement with values reported in the literature. The curves in Figure 1(b) are a result of the application of the Henderson-Hasselbalch equation. For methyl orange we developed a simple theoretical description based on a two-level model to account for the results.[5]

In summary, we have described the application of the *Z*-scan technique to determine pK values in a chemical process. The results show that either the nonlinear refraction or the nonlinear absorption processes can be exploited to determine pK. Using methyl orange, a well-known pH indicator, as a test system, we demonstrated that pK can be well determined through the third-order susceptibility changes. Also, since the *Z*-scan technique is sensitive, we expect that the method devised here will find many applications in the study of organics and other biomaterials.

References

1. Y. R. Shen, The Principles of Nonlinear Optics (Wiley, New York, 1984).
2. X. D. Xiao, V. Vogel, Y. R. Shen, and G. Marowsky, "Molecular monolayers of charge-transfer molecules: protononation and aggregation studied by second harmonic generation" J. Chem. Phys. **94**, 2315-23 (1991).
3. M. Sheik-Bahae, A. A. Said, and E. W. van Stryland, "High-sensitivity, single-beam n_2 measurements," Opt. Lett **14**, 955-7 (1989).
4. A. G. Bezerra, Jr., I. E. Borissevitch, A. S. L. Gomes, and C. B. de Araújo, "Exploitation of the Z-scan technique as a method to optically probe pK_a in organic materials: application to porphyrin derivatives," Opt. Lett. **25**, 323-5 (2000).
5. R. E. de Araujo, A. S. L. Gomes, and Cid B. de Araújo, "Measurements of pK_a of organic molecules using third order nonlinear optics," Chem. Phys. Lett. **330**, 347-53 (2000).

Optical Design

Cost-Based Tolerancing of Optical Systems

By Richard N. Youngworth and Bryan D. Stone

The manufacturing tolerances assigned to an optical system have significant impact on the ultimate cost of production. Consequently, the step of assigning tolerances is critical. The ultimate goal is to assign tolerances such that the as-built systems satisfy all required specifications and possess the lowest cost to produce. In general, tight tolerances lead to improved yield (better image quality for as-built systems), but higher cost. Conversely, loose tolerances lead to lower yield but less expensive systems to fabricate. In his dissertation over ten years ago, Geoff Adams recognized the need for improved tolerancing methods and, ultimately, cost-based tolerance optimization.[1] More recently, in an article for OPN,[2] Doug Sinclair pointed out that optics is no longer a "service discipline for other sciences." Instead, he noted that it is "rapidly becoming a consumer technology," for which systems must be not only good, but also cost effective. In his article, he further states that tolerancing is "the most challenging and traditionally the most neglected aspect of optical design."

The current state of tolerance analysis requires a high degree of skill and experience to even hope to attain the cheapest possible set of tolerances that still provides the desired image quality. With the extreme complexity of many current designs, a rigorous modern design method is necessary to cope with the problem. We recently reported a method for assigning manufacturing tolerances[3] that has a number of advantages over current methods. The approach is analogous to conventional optimization of imaging systems (a tool that is an essential feature of any modern lens design software). In our case, however, the figure of merit is replaced by a cost function with two components. The cost to produce the system with a given set of tolerances comprises the first component. The second component is composed of the cost for systems that are rejected (i.e., manufactured systems that do not possess adequate image quality).

The first component—the costs associated with any given set of tolerances—is required for any cost–based tolerancing method. This information is not readily available for all optics shops, but current trends toward greater process control (see, for example, Willey's work in Ref. 4) lead to improved modeling of fabrication methods. The second component—the cost of rejected systems—requires knowledge of the distribution of the image quality of as-built systems. Furthermore, this distribution must be determined efficiently enough so that it can be part of a larger optimization loop. We have devised a means of estimating the as-built imagery (associated with any given set of tolerances) that is both fast and accurate. With the ability to determine quickly the overall cost associated with any given set of tolerances, it is then relatively straightforward to optimize that cost for any given design. In Ref. 1, an example is presented showing how the optimal tolerances for a system change as the costs of meeting tolerances and the costs of rejecting systems are varied. By accounting for both the manufacturing costs and the costs of rejected systems, the proposed method for tolerance assignment can be applied to a wide variety of applications: from low precision, high volume; to high precision, low volume.

References

1. G. Adams, "Tolerancing of optical systems," Ph.D. dissertation (Imperial College, University of London, London, 1987).
2. D. C. Sinclair, "Whither optical design," Opt. Photon. News, **11** (6), 34-5, 38-9 (June 1999).
3. R. N. Youngworth and B. D. Stone, "Cost-based tolerancing of optical systems," Appl. Opt. **39**, 4501-12 (2000).
4. R. R. Willey and R. E. Parks, "Dimensional tolerances and budgets," in Handbook of Optomechanical Engineering, A. Ahmad, ed. (CRC Press, Boca Raton, Fla., 1997), pp. 14-38.

Imaging with Spherical Mirrors

By Joseph M. Howard and Bryan D. Stone

Imaging systems composed solely of reflecting elements have several advantages over refractive designs for certain applications. They introduce no chromatic aberrations, enabling a much wider spectral band than similar refractive systems. Furthermore, at wavelengths shorter than approximately 150 nm, refractive materials that transmit are scarce to nonexistent, leaving reflecting systems as the only option. Another advantage is that mirrors generally weigh less and need relatively simpler fabrication and mounting methods for applications that require larger optics.

Previous approaches to the design of all-reflective optical systems have varied. Although many designs incorporate aspheric elements (such as the familiar Cassegrain telescope), the advantages of spherical surfaces for fabrication and testing make their use attractive. Even when aspheric mirrors are used, it is still desirable to manufacture and test a relatively small aspheric departure of the reflecting surface. Therefore, a reasonably well-corrected design with spherical mirrors can be advantageous as a starting point for further optimization.

We recently reported on methods for performing design studies of unobstructed systems of three and four spherical mirrors.[1,2] These papers supplement earlier research on two spherical mirror imaging systems.[3] The basic approach that we use is to exclude explicitly from consideration any system that does not possess the appropriate first-order imaging properties for the intended application. This in turn leads to a reduction in the dimensionality of the resulting design space. These ideas facilitate the design process tremendously and thereby present the best chance of finding the optimal configuration of such three and four mirror systems for a given application. Note that the method can be applied to a variety of applications that require spherical mirror systems (either as the final design or as a starting point). The systems can operate at finite conjugates or with the object at infinity and with any speed and field of view.

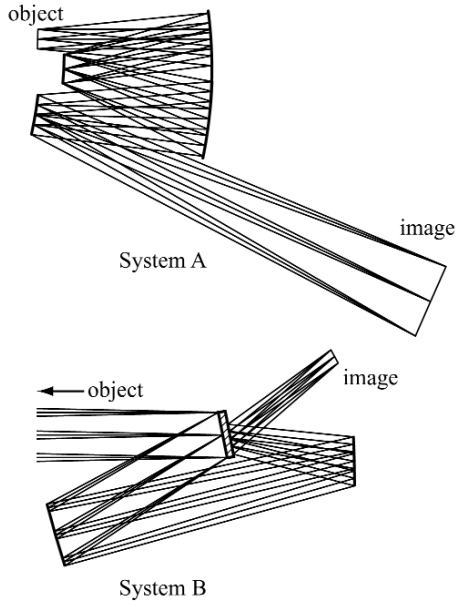

Imaging with Spherical Mirrors Figure 1. The cross section through the plane of symmetry for two unobstructed spherical mirror systems (labeled System A and System B). Four spherical mirrors comprise each system.

In Refs. 1 and 2, a variety of sample design studies are presented. In one example described in Ref. 1, we were able to find all the design forms that appear in a disparate set of papers on three-spherical-mirror imaging systems. The ability to unify the results of previous research into these types of system is one demonstration of the utility of this approach. Conventional systems were also found in a separate design study presented in Ref. 2. More importantly, however, a variety of interesting and unconventional forms were discovered. Two examples are shown in Figure 1. The first, labeled System A, operates at finite conjugates. For this system, the first and third mirrors possess the same radius of curvature and the same center of curvature, that is, a single mirror can be used for the first and third reflections. System B is a variation of this idea. In this system, however, the first and fourth mirrors could be made from a single substrate with the mirrors on opposite sides. The ability to uncover new design forms represents the real power of these methods.

References

1. J. M. Howard and B. D. Stone, "Imaging with three spherical mirrors," Appl. Opt. **39**, 3216-31 (2000).
2. J. M. Howard and B. D. Stone, "Imaging with four spherical mirrors," Appl. Opt. **39**, 3232-42 (2000).
3. J. M. Howard and B. D. Stone, "Imaging a point with two spherical mirrors," J. Opt. Soc. Am. A **15**, 3045-56 (1998).

Laser-Diode Modelization In Optical Design Software

By Simon Thibault

The term laser diode is quite well known in optics. Communication industries, medical science, and numerous other areas of science use it for many applications. Until recently, the simulation of this kind of device seemed to be simple. Specialists in optical design would tell you that that is not the case. The problem exists because more and more nonoptical designers work with optical design software. Optical design software is easy to use because it has a simple graphical user interface and a powerful optimization routine. By optimization I mean the process of balancing aberration to achieve good image quality. In general, an optical engineer (rather than an optical designer) uses the default merit function (MF), which is a good choice for solving a wide range of problems. However, the default MF is often a poor choice because of the garbage in—garbage out principle. What happens is that the computer attempts to optimize something that cannot be optimized. A good example is a laser diode source modelization.

To simulate a laser-diode source, the suggestion of astigmatic distance[1] has been made such that the diode

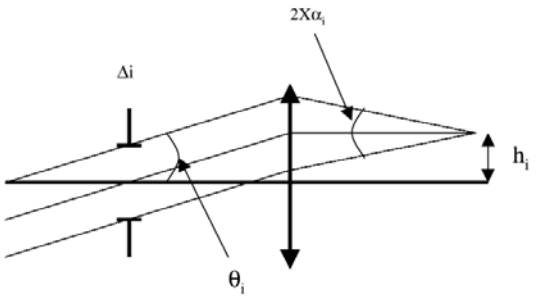

Laser-Diode Modelizaton Figure 1. A telecentric optical system.

resembles two point sources. The ultimate result is to collimate a high-power laser diode at 810 nm and inject it into a 100-μm fiber core with a numerical aperture of 0.2. The laser diode has a 1μm x 100 μm emitting area with 40° x 10° angles of divergence. The design was created with ZEMAX^R-EE Version 8.0. After optimization by use of the default MF, the spot diagram measured less than 10 μm in both axes. Based on this model, the conclusion is that a laser diode can be coupled into 100-μm fiber without a significant loss of power. However, this result does not correspond to the experiment.

We can now create the same optimization by using our new model,[2] which is based on the telecentric system, as illustrated in Figure 1. The diode laser can be defined by

$$h_i = f \tan \theta_i \qquad (1),$$

$$\tan \alpha_i = \frac{\Delta i}{2f} \quad , \qquad (2)$$

where h_i is the size, Δi is the stop size, α_i is the half-divergence angle, f is the focal length of the telecentric lens, and θ_i is the field angle in the i direction (x or y). With this approach, the spot size after optimization with the same default MF as before is essentially 200 μm in the slow axis and nearly 10 μm in the fast axis. This result has been confirmed by experimental verification. So this simple way to deal with a laser diode allows us to use the default MF during the optimization process.

This technique would be useful to optical engineers and optical designers at all levels of experience. This technique might also lead other researchers to examine optical design software from a new perspective.

References

1. "Diode laser assembly," in Melles Griot 1995-1996 catalog (1995), Chap. 48, pp. 48-55.
2. S. Thibault, "Astigmatic light source in optical design software," Opt. Eng. **39** (7), 1808-11 (2000).

Optical Vortices

Parametric Optical-Vortex Solitons

By Paolo Di Trapani, Gintaras Valiulis, Yuri S. Kivshar and Tristram J. Alexander

An optical vortex is associated with a beam that carries a phase singularity on an electromagnetic field so that the beam intensity vanishes at a certain point and the field phase changes by $2\pi\ m$ (m being an integer) along any closed loop around the zero-intensity point. This type of *wave dislocation*[1] has been generated and observed in different optical media, where it has also been shown that the diffraction-induced expansion of the vortex core can be compensated for by the nonlinear response of the medium. In self-defocusing optical media this nonlinearity-induced change of the refractive index leads to a stationary self-trapped state—an *optical-vortex soliton*. A deep analogy between optical vortices and linear topological defects in superfluids has already been established for scalar fields.[2] However, the recent experimental observation[3] of a rich variety of exotic types of topological defects in unconventional superfluids (and superconductors) has prompted a search for much deeper analogies between superfluids and optics, where vortices and vortex solitons can appear in parametrically coupled vector fields.

What is believed to be the first theoretical analysis of parametric vortex solitons, recently carried out by Alexander *et al.*,[4] demonstrated that multicomponent optical vortices and vortex solitons possess unexpected complex properties. These properties were found to be even more exotic and somewhat more rich in comparison with their cousins, quantized vortices in superconductors and unconventional superfluids such as 3He-A. Many new features were also discovered in that study. In particular, as was shown in Ref. 4, parametric modulational instability can easily destroy optical vortices by a strong modulation of the background beam, leading to their subsequent disintegration. This should make optical vortices difficult to see in an experiment. Nevertheless, the first successful experimental observation of two-component parametric vortex solitons was recently reported by Di Trapani *et al.*,[5] who employed a com-

Parametric Optical-Vortex Solitons Figure 1. Vortex-soliton achievement. (a) FH intensity profile at the crystal input face, (b) diffracted FH output in regime of linear propagation, (c) FH output in the soliton regime, (d) SH output in the soliton regime. Arrows, oriented in the walk-off direction, indicate the position of the vortex singularity.

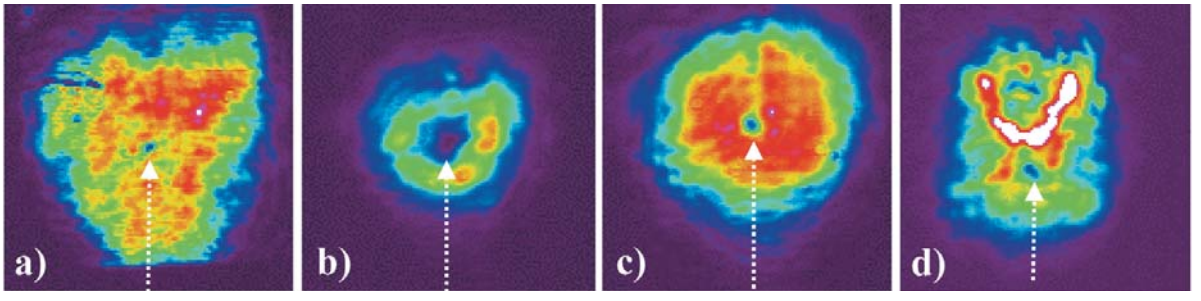

bined effect of transversal walk-off and finite beam size to eliminate the dangerous development of modulational instability.

Figure 1 shows the experimental results in the presence of walk-off. An optical vortex at the fundamental harmonic (FH) [see Fig. 1(a) for the input profile] propagates through a 30-mm-long lithium triborate crystal, generating a second-harmonic (SH) double-charge vortex by means of a type I SH-generation (SHG) parametric process. At low input intensity (linear regime) both vortices experience strong diffraction [see Fig. 1(b) for the FH case]. At high intensity (I = 30 GW/cm^2) an effective self-defocusing SHG cascading process allows for the formation of a vortex soliton, which consists of two coupled fields propagating in the absence of (core) diffraction [see FH and SH output profiles shown in Figs. 1(c) and 1(d), respectively].

This demonstration represents what we believe is the first achievement of a *stable localized structure* in parametric wave mixing that carries *angular momentum*. This will guide a deeper understanding of the structure and stability of multicomponent optical phase dislocations in nonlinear coupled fields and should be studied in analogy with the counterparts in superfluids.

References and Notes

1. J. F. Nye, Natural Focusing and Fine Structure of Light: Caustics and Wave Dislocations (Institute of Physics, Bristol, UK, 1999).
2. See, e.g., Yu. S. Kivshar and B. Luther-Davies, "Optical dark solitons: physics and applications," Phys. Rep. **298**, 81-197 (1998).
3. See, e.g., O. V. Lounasmaa and E. Thuneberg, "Vortices in rotating superfluid 3He," Proc. Natl. Acad. Sci. USA **96**, 7760-7 (1999).
4. T. J. Alexander, Yu. S. Kivshar, A. V. Buryak, and R. A. Sammut, "Optical vortex solitons in parametric wave mixing," Phys. Rev. E **61**, 2042-9 (2000).
5. P. Di Trapani, W. Cinaglia, S. Minardi, A. Piskarskas, and G. Valiulis, "Observation of quadratic optical vortex solitons," Phys. Rev. Lett. **84**, 3843-6 (2000).

Nonlinear Aharonov-Bohm Effect On Optical Vortices

By Yuri Kivshar, Alex Nepomnyashchy, Vladimir Tikhonenko, Jason Christou, and Barry Luther-Davies

Optical vortices,[1] phase dislocations, or phase defects of electromagnetic waves are fundamental in singular optics. They are a unique class of objects that introduce new concepts into the physics of light linking it to superfluids and Bose-Einstein condensates. Recent progress in singular optics has been associated with the study of nonlinear effects, such as frequency conversion, self-trapping of light, and spatial optical vortex solitons.[2]

From a broader perspective, the study of optical vortices allows a strong analogy to be drawn between seemingly different fields of physics, leading to some interesting and unexpected predictions in optics. One such effect, which we can now identify as the nonlinear Aharonov-Bohm effect, has recently been predicted theoretically and observed experimentally for optical vortices generated in a nonlinear medium composed of atomic-rubidium vapor.[3]

When applied to the physics of vortices, the (linear) Aharonov-Bohm (AB) effect is known as splitting a wave front at the vortex,[4] which is similar to the formation of dislocations in crystals or striped optical patterns. If we consider a small-amplitude wave packet that is scattered by a vortex, the AB effect is the result of an accumulated shift of a wave front that is due to the effect of its advection by a vortex-induced phase-field gradient.[4] In a nonlinear case, one can consider the analogous problem of scattering of a dark-soliton stripe (the so-called nonlinear localized wave packet) by an optical vortex or vortex soliton. In the small-amplitude limit, such scattering results in a simple wave-front shift, a linear AB effect. However, when the stripe amplitude increases, the shift increases and becomes amplitude dependent. In addition, the wave-front splitting initiates the development of transverse modulational instability of the dark-soliton stripe,[5] thereby providing a strong manifestation of a nonlinear AB effect. Figure 1 shows the experimental study of the vortex-stripe interaction by use of a cw Ti:sapphire laser and a defocusing nonlinear medium composed of atomic-rubidium vapor. We created a vortex by imaging the waist of a linearly polarized Gaussian beam onto a computer-generated phase mask, thereby introducing a singly charged phase dislocation into the wave front. The beam waist and dislocation were then imaged onto the input window of the nonlinear medium—a 20-cm-long cell that contained atomic-rubidium vapor, creating an optical vortex at any desired position [see Figure 1(a)]. In addition a dark-soliton stripe was created by a π phase jump imposed across the beam center by a phase-shifting mask [see Figure 1(b)].

When both the vortex and the stripe were created simultaneously so that they interacted in the nonlinear medium, the stripe bent and, for larger nonlinearity (which was controlled by the frequency detuning of the laser relative to the atomic absorption line), this bending and wave-front shift initiated the stripe break-up, as shown in Figure 1(c) and 1(d). Thus, the presence of the vortex induced a phase difference that is proportional to the vortex circulation, which leads to the asymmetric amplitude modulation, initiating the stripe transverse instability, a remarkable nonlinear effect.

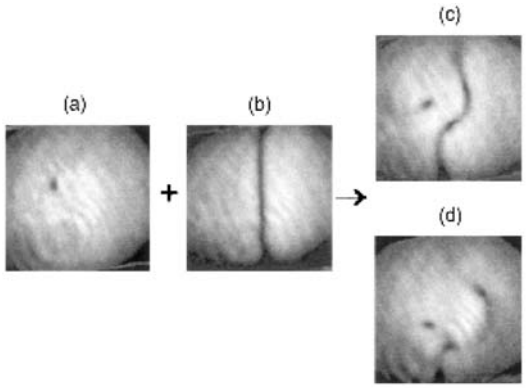

Nonlinear Aharonov-Bohm Effect Figure 1. Experimental images of a vortex interacting with a dark-soliton stripe.[3] (a) The output position of the vortex without the stripe and (b) the stripe background without a vortex. When the vortex is embedded in the stripe background, the interaction leads to the stripe bending, the vortex downshifting [see (c)], and the subsequent stripe breakup into component vortices [see (d)].

Acknowledgment

The work was supported by the Australian Photonics Cooperative Research Centre and by the Performance and Planning Fund.

References

1. M. Vasnetsov and K. Staliunas, eds., Optical Vortices (Nova Science, New York, 1999).
2. Yu. S. Kivshar and B. Luther-Davies, "Dark optical solitons: Physics and applications," Phys. Rep. **298**, 81-197 (1998).
3. Yu. S. Kivshar, A. Nepomnyashchy, V. Tikhonenko, J. Christou, and B. Luther-Davies, "Vortex-stripe soliton interaction," Opt. Lett. **25**, 123-5 (2000).
4. L. M. Pismen, Vortices in Nonlinear Fields (Oxford, Oxford, London, 1999).
5. Yu.S. Kivshar and D.E. Pelinovsky, "Self-focusing and transverse instabilities of solitary waves," Phys. Rep. **331**, 117-84 (2000).

PHOTONIC BANDGAP STRUCTURES

Hexagonal Resonators for Molecular Sieve Microlasers

By Lhoucine Benmohammadi, Ingo Braun, Franco Laeri, Jens Uwe Nöckel, Günther Schulz-Ekloff, Ferdi Schüth, Uwe Vietze, Özlem Weiss, Dieter Wöhrle

Molecular sieves are crystalline solid-state materials with crystallographically defined nanometer-size pores. This property stimulates attempts to use the sieves as an inert ordering framework for the arrangement of optically functional molecules, to create a compound material with new optical properties. For example, many organic molecules with large nonlinear hyperpolarizability crystallize in a centrosymmetric structure, and as a result the macroscopic even-order susceptibilities vanish. It has been shown that such molecules can be arranged in molecular sieves with a noncentrosymmetric symmetry.[1]

Based on this idea, we investigated the aluminophosphate sieve, $ALPO_4$-5, which exhibits channellike pores with a diameter of 0.73 nm, which is sufficiently large to consider the inclusion of some organic laser dyes. In Ref. 2 we reported laser action in the $ALPO_4$-5 molecular sieve, in which the dye 1-ethyl-4-(4-(p-dimethylaminophenyl)-1,3-butadienyl)-pyridinium perchlorate (pyridine 2) was caged. In Ref. 3 we discussed the results with derivatives of Rhodamine dyes. With an approximate diameter of 0.69 nm, pyridine 2 molecules align with the 0.73-nm-wide channel pores of the $ALPO_4$-5 molecular sieve, which acquires strong dichroic and birefringent properties. Lasing in this compound material occurs in micrometer-size ring resonators, in which the laser mode is confined by total internal reflection at the natural hexagonal crystal side faces such as in a whispering gallery mode. Inasmuch as the compounds are synthesized by the inexpensive method of hydrothermal growth, we have already been successful in obtaining several grams of microlasers or lasing powder.

Figure 1(a) is a schematic picture of the whispering gallery lasing mode in a hexagonally bounded dielectric prism. In contrast with this picture, the experiment clearly revealed that the laser light exits from the prism resonator at the edges. The main feature that distinguishes the hexagonal resonator from other common whispering gallery type cavities, such as microdroplets or disk lasers, is that the latter do not exhibit sharp corners and flat sides. The hexagon in fact constitutes a self-assembled realization of a pseudointegrable structure.

An orthogonal coordinate system in which the wave equation can be solved by separation of variables does not exist. Figure 1(b) shows the result of a numerical simulation of the field distribution of a counterclockwise propagating mode with 685-nm wavelength in a hexagon with a 4.5-μm width over flats. The simulation correctly reproduces the outcoupling location of the field at the corners. Upon closer examination one can see that the number of ridges and nodal lines is not uniquely defined (optical defects). As a result, the modes in a hexagonal resonator cannot be labeled properly by good quantum numbers, which is a direct consequence of the nonintegrability of the problem.

The photostability of organic dyes is a critical issue. In traditional, liquid dye lasers, photobleaching is irreversible. Strong pumping bleaches the caged dye molecules as well. However, we observed that the fluorescence of caged pyridine 2 molecules recovers with a time constant of approximately 2 min. The physical mechanism behind this recovery is not yet understood.

References

1. S. D. Cox, T. E. Gier, G. D. Stucky, and J. Bierlein, "Inclusion tuning of nonlinear optical materials: switching the SHG of p-nitroaniline and 2-methyl-p-nitroaniline with molecular sieve hosts," J. Am. Chem. Soc. **110**, 2986-7 (1988).
2. U. Vietze, O. Krauss, F. Laeri, G. Ihlein, F. Schüth, B. Limburg, and M. Abraham, "Zeolithe-dye microlasers," Phys. Rev. Lett. **81**, 4628-31 (1998).
3. I. Braun, G. Ihlein, F. Laeri, J. U. Nöckel, G. Schulz-Ekloff, F. Schüth, U. Vietze, Ö. Weiss, and D. Wöhrle, "Hexagonal microlasers based on organic dyes in a nonoporous crystal," Appl. Phys. B **70**, 335-43 (2000).

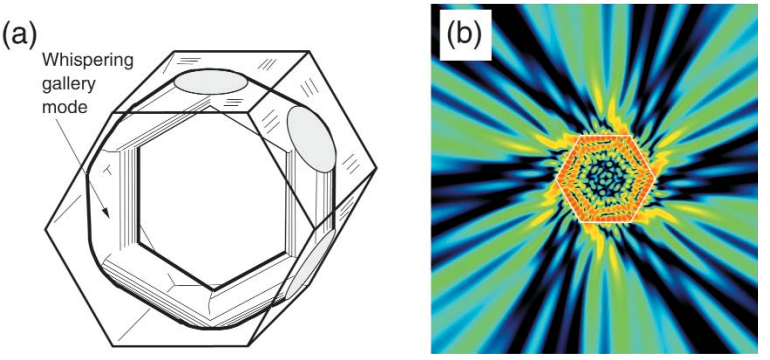

Hexagonal Resonators Figure 1. (a) Schematic representation of the lasing mode in a hexagonal ring resonator. (b) Numerical simulation of the field distribution in a hexagonal dielectric resonator with 685-nm wavelength and a 4.5-μm hexagonal width over flats.

Bacteriorhodopsin: A Natural (Nonlinear) Photonic Bandgap Material

By Koen Clays, Sven Van Elshocht, and André Persoons

Photonic bandgap materials, often also called photonic crystals, are engineered materials with a periodicity in dielectric properties.[1] This periodicity results in a range of forbidden energies for a photon: Photons with a wavelength in the corresponding photonic bandgap cannot propagate through the material. Recently, second-harmonic generation has been realized in a photonic crystal.[2] In a nonlinear photonic crystal, the optical nonlinearity of the harmonic-generating material (the hyperpolarizability) is decoupled from the linear optical properties (the refractive index). This has important consequences on phase-matching schemes for efficient nonlinear conversion in these materials.

The purple membrane of *Halobacterium halobium* has received considerable attention as a candidate material for optical information processing. The two-dimensional purple membrane consists of patches of the protein bacteriorhodopsin. The small optical moiety, the retinal chromophore, is embedded in this large protein matrix. The molecular hyperpolarizability of retinal and derivatives was analyzed previously both theoretically and experimentally.[3] The second-order nonlinear optical properties of the protein could be experimentally determined by means of hyper-Rayleigh scattering.[4]

We have now studied the angular dependence of the hyper-Rayleigh scattering as a function of time during the ongoing process of the solubilization. In Fig. 1 we show the angular dependence that is observed before any solubilization takes place. The solid curve is a fit to a theoretical model that accounts for both coherent and incoherent contributions to the hyper-Rayleigh signal. The coherent contribution can be described by a sinc^2 function [$\mathrm{sinc}(x) = \sin(x)/x$]. The argument x of the function, $(4\pi L_{coh}/\lambda)\overline{n_\omega n_{2\omega}}\sin\theta/2$, is determined by the coherence length L_{coh} for coherent second-harmonic generation and by the refractive index n at both fundamental ω and second-harmonic wavelength 2ω. The intensity of the hyper-Rayleigh signal at an angle θ is also determined by the optical nonlinearity at the fundamental wavelength λ of the retinal itself. The best fit to the experimental data (the solid curve in Fig. 1) is found by combination of the nonlinear optical properties (the hyperpolarizability) of only the small retinal moiety with the linear optical properties (the refractive index) of the large protein matrix. Therefore we can, for the first time to our knowledge, attribute nonlinear photonic bandgap properties to this natural material.[5]

This has important consequences, since all photonic bandgap materials reported so far exhibit a high degree of order and are, therefore, artificially engineered structures. Crystals of bacteriorhodopsin are self-assembled nonlinear photonic crystals with a coherence length that is limited only by the physical size of the crystal. Genetic engineering and counter-ion position modulation can fine tune the relevant properties for a specific application.

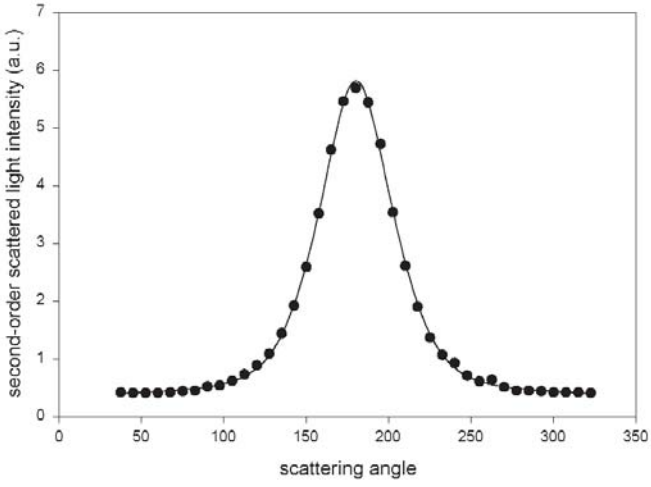

Bacteriorhodopsin Figure 1. Angular dependence of second-harmonic light intensity scattered by a suspension of purple membrane before any solubilization.

References

1. J. D. Joannopoulos, P. R. Villeneuve, and S. Fan, "Photonic crystals: putting a new twist on light," Nature **386**, 143-9 (1997).
2. J. Martorell, R. Vilaseca, and R. Corbalán, "Second harmonic generation in a photonic crystal," Appl. Phys. Lett. **70**, 702-4 (1997).
3. E. Hendrickx, K. Clays, A. Persoons, C. Dehu, and J.-L. Brédas, "The bacteriorhodopsin chromophore retinal and derivatives: an experimental and theoretical investigation of the second-order optical properties," J. Am. Chem. Soc. **117**, 3547-55 (1995).
4. K. Clays, E. Hendrickx, M. Triest, T. Verbiest, A. Persoons, C. Dehu, and J.-L. Brédas, "Nonlinear optical properties of proteins measured by hyper-Rayleigh scattering in solution," Science **262**, 1419-22 (1993).
5. K. Clays, S. Van Elshocht, and A. Persoons, "Bacteriorhodopsin: a natural (nonlinear) photonic bandgap material," Opt. Lett. **25**, 1391-3 (2000).

PHOTONIC CRYSTALS

Propagation of Photons by Hopping

By Mehmet Bayindir and Ekmel Özbay

By breaking the periodicity of photonic crystals, it is possible for one to create highly localized defect modes within the stop band.[1] If we provide enough overlap between cavity modes, photons can hop from one cavity to the neighboring cavity, as illustrated in Fig. 1(a), which can be considered as the classical wave analog of the tight-binding (TB) approximation in solid-state physics. This novel waveguiding mechanism, which we call the coupled-cavity waveguide (CCW),[2-5] has a pivotal role in overcoming the problem of guiding light around sharp corners in optoelectronic components and circuits. Conventional metallic or dielectric waveguides undergo significant radiation loss when sharp bends are introduced.

First, we demonstrate CCWs at microwave frequencies by using layer-by-layer dielectric-based three-dimensional photonic crystals.[2-4] We formed the cavities by removing a single rod from each unit cell of the crystal. Fig. 1(b) (red) displays the transmission characteristics of a ten-unit cell zigzag CCW [see Fig. 1(b) inset]. A guiding band or defect band was formed with-

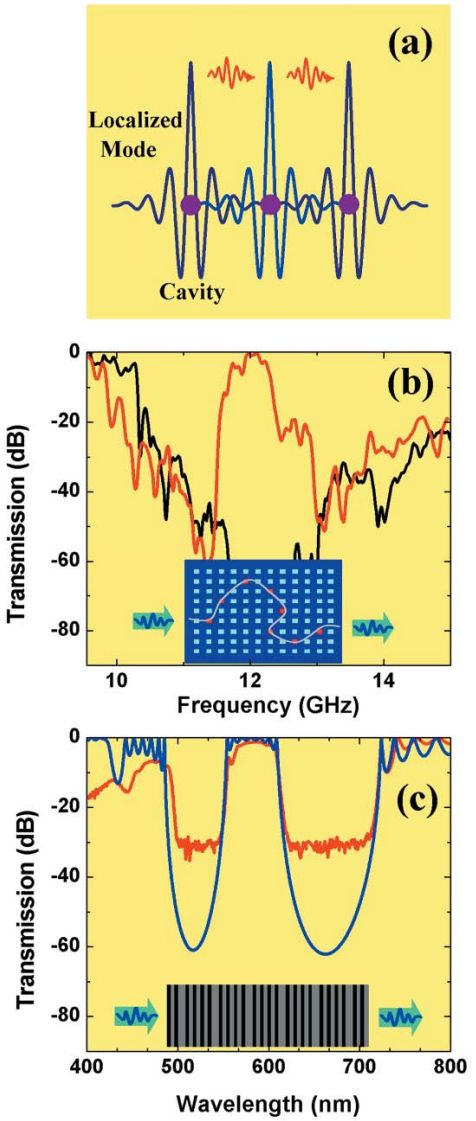

Propagation of Photons Figure 1. (a) Schematic of the propagation of photons through localized coupled-cavity modes within a photonic bandgap structure. (b) Transmission characteristics of a zigzag CCW (red) and a perfect photonic crystal (black). (c) Measured (red) and calculated (blue) transmissions through the silicon-oxide/silicon-nitrite pairs with silicon-oxide cavity layers.

in the photonic bandgap because of the interaction between localized cavity modes. Almost complete transmission of the electromagnetic wave was achieved throughout the waveguiding band regardless of the direction of propagation. The transmission spectrum of the perfect crystal (black) is also plotted for comparison.

Since the Maxwell equations have no fundamental length scale, our microwave and millimeter wave results can be extended to optical frequencies. We observed the guiding of light through localized optical cavity modes in one-dimensional photonic bandgap structures that were fabricated with silicon-oxide/silicon-nitrite pairs with silicon-oxide cavity layers [see Fig. 1(c) inset]. As shown in Fig. 1(c) (red), nearly 100% transmission was measured throughout the cavity band. The theoretical results (blue) obtained from the transfer matrix method simulations are in good agreement with the measurements.

We can also report that the group velocity tends toward zero and the photon lifetime increases drastically at the CCW band edges. This observation has practical importance, inasmuch as the efficiency of nonlinear processes can be increased because of low group velocity and large optical field amplitude. At the CCW band edges, both requirements are satisfied simultaneously. Moreover, the spontaneous emission can be enhanced at the CCW band edges. It is also important to note that all the experimental results, namely, dispersion relation, group velocity, and photon lifetime, agree well with the prediction of the TB photon picture.

Acknowledgments

This research was supported by Turkish Department of Defense grant KOBRA-001 and Thales JP8.04, NATO grant SfP971970, and National Science Foundation grant INT-9820646.

References

1. J. D. Joannopoulos, R. D. Meade, and J. N. Winn, Photonic Crystals: Molding the Flow of Light (Princeton U. Press, Princeton, N.J., 1995).
2. M. Bayindir, B. Temelkuran, and E. Özbay, "Tight-binding description of the coupled defect modes in three-dimensional photonic crystals," Phys. Rev. Lett. **84**, 2140-3 (2000).
3. M. Bayindir, B. Temelkuran, and E. Özbay, "Propagation of photons by hopping: a waveguiding mechanism through localized coupled-cavities in three-dimensional photonic crystals," Phys. Rev. B **61**, R11855-8 (2000).
4. M. Bayindir and E. Özbay, "Heavy photons at coupled-cavity waveguide band edges in a three-dimensional photonic crystal," Phys. Rev. B **62**, R2247-50 (2000).

Guiding Mechanism in Photonic Crystal Fibers

By Albert Ferrando, Enrique Silvestre, Juan José Miret, Pedro Andrés, and Miguel V. Andrés

Photonic crystal fibers (PCFs) are thin silica glass fibers that possess a regular array of microscopic air holes that extend along the entire fiber length. For certain geometries PCFs present a photonic bandgap structure. Light propagation is forbidden within the bandgaps, whereas conduction bands are constituted by radiative modes.

The most common PCF comprises a triangular two-dimensional air-hole lattice with a missing central hole.[1] In this structure the dispersion relation of guided modes appears in the semiinfinite forbidden band whose lower bound is determined by the lowest-order Bloch mode that can propagate in the periodic structure.[2] Inasmuch as this bound determines the effective cladding index that is lower than that of the core, this nonintraband guidance is considered by some authors as having been produced by total internal reflection (TIR).

Alternatively, guidance is also possible in honeycomb PCF structures in which the defect is generated by an off-lattice air hole. Here the guided modes lie on the forbidden band that exists between the first two conduction bands of the honeycomb photonic-crystal cladding.[3,4] Inasmuch as the average index of the cladding is now higher than the refractive index of the airhole defect core, guidance cannot be interpreted in terms of a TIR mechanism. Instead, the intraband guid-

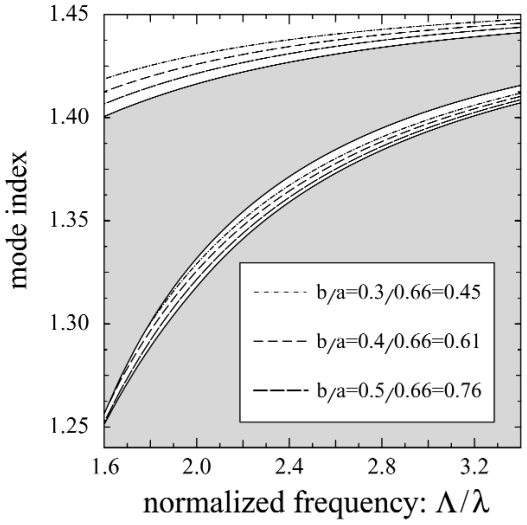

Guiding Mechanism in Photonic Crystal Fibers Figure 1. Modal dispersion curve for some donor-guided modes for three different defect radii. In all cases, the air-filling fraction of the PCF structure is $f = (2\pi/\sqrt{3})(a/\Lambda)^2$, where Λ denotes the pitch between consecutive holes.

ing mechanism is attributed to the inhibition of transverse radiation produced by the forbidden band of the photonic-crystal cladding. This mechanism is referred to as photonic bandgap guidance (PBG).

We accomplished an in-depth study of the guiding mechanism of PCFs. We introduced an irregularity in a perfectly periodic triangular structure of circular air holes (of radius *a*) by decreasing or increasing the size of the central hole (of radius *b*). The sign of the local variation of the refractive index determines the character of the defect, which acts as a donor impurity in an electron crystal for a positive index variation ($b < a$) and as an acceptor impurity for a negative index variation ($b > a$). For an acceptor defect ($b > a$), the localization mechanism causes a state to leave the upper conduction band and to enter the forbidden band located just below, as in a honeycomb PCF.

Alternatively, if we decrease the size of the defect ($b < a$), guided modes are promoted into the forbidden bands from neighboring conduction bands. However, unlike in the acceptor defect case, these guided modes originate in the immediately lower conduction bands. We have recognized several configurations in which guided modes appear simultaneously in both the upper and the lower forbidden bands of the triangular photonic crystal,[5] as shown in Fig. 1.

In light of the existence of these donor configurations that simultaneously present intraband and nonintraband guided modes, it seems unnatural to interpret PCF guidance by invoking two different physical principles to occur in the same structure at the same time. This is especially true when these guided modes are simultaneously promoted into the upper and the lower forbidden bands by an identical mechanism. In view of these results, we conclude that the guiding mechanism in PCFs is always provided by a unique phenomenon of multiple interference by the periodic structure, which does not distinguish between upper and lower forbidden band guidance.

Acknowledgment

This study was financially supported by the Generalitat Valenciana, grant GV96-D-CN-05141, Spain.

References

1. J.C. Knight, T. A. Birks, P. St. J. Russell, and D. M. Atkin, "All-silica single-mode optical fiber with photonic crystal cladding," Opt. Lett. **21**, 1547-9 (1996).
2. A. Ferrando, E. Silvestre, J. J. Miret, and P. Andrés, "Full-vector analysis of a realistic photonic crystal fiber," Opt. Lett. **24**, 276-8 (1999).
3. J.C. Knight, J. Broeng, T. A. Birks, and P. St. J. Russell, "Photonic band gap guidance in optical fibers," Science **282**, 1476-8 (1998).
4. S.E. Barkou, J. Broeng, and A. Bjarklev, "Silica-air photonic crystal fiber design that permits waveguiding by a true photonic bandgap effect," Opt. Lett. **24**, 46-8 (1999).
5. A. Ferrando, E. Silvestre, J. J. Miret, P. Andrés, and M. V. Andrés, "Donor and acceptor guided modes in photonic crystal fibers," Opt. Lett. **25**, 1328-30 (2000).

Nonlinear Localized Modes In Photonic Crystal Waveguides

By Serge F. Mingaleev, Yuri S. Kivshar, Rowland A. Sammut

Photonic technology, by use of light instead of relatively slow electrons as the information carrier, is increasingly being proposed as a replacement for electronics in communication and information management systems. Among the most promising optical materials for achieving this goal are *photonic bandgap crystals*, in which periodic modulation of a dielectric constant controllably prohibits electromagnetic propagation throughout a specified frequency band.[1] Recent dramatic success in fabrication of photonic crystals with a bandgap at optical wavelengths[2] renders investigation of their properties a central problem.

Of special interest among the devices for microscopic light manipulation which have been proposed on the basis of photonic bandgap materials are carefully engineered line defects which could act as *waveguides* inside all-optical microchips. Very recently, Tokushima *et al.*[3] demonstrated highly efficient propagation of 1.55 μm wavelength light through a 120° sharply bent waveguide formed in a triangular lattice two-dimensional (2D) photonic crystal.

But to employ the high-tech potential of photonic crystal waveguides, it is important to achieve a dynamical tunability of their properties. This idea can be realized by changing the light intensity in the case of photonic crystals composed of a material with a *nonlinear response*[4] or photonic crystals with embedded *nonlinear impurities*. In this case the high-intensity light can propagate through the waveguide in the form of *nonlinear localized mode*.[5]

For instance, let us consider a 2D photonic crystal created by a square lattice of parallel, infinitely long dielectric rods in air, with a waveguide created by inserting an additional row of rods (the top view of such a structure is depicted at the top of Fig. 1). If the rods are fabricated from a Kerr-type nonlinear material, the electromagnetic field can be localized in the *waveguide direction*, totally due to the nonlinearity. At the top of Fig. 1 we plot the electric field E of the corresponding nonlin-

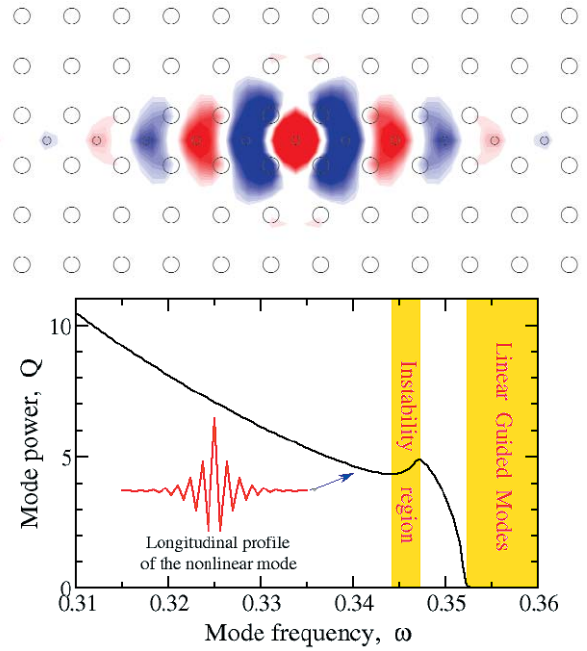

Nonlinear Localized Modes Figure 1. Electric field distribution of the nonlinear localized mode excited in the photonic crystal waveguide (top) and the dependence of the mode power on the frequency (bottom). The mode is unstable in the shaded region due to the effctive nonlocal interaction between waveguide rods.

ear localized mode. The most important physical characteristic of such a mode is its power Q (which is closely related to the mode energy) depicted at the bottom of Fig. 1 as a function of the mode frequency (all the frequencies in Fig. 1 lie inside the bandgap). Importantly, *stability* of such a localized mode is determined by the slope of the dependence Q(ω): the mode is stable when this slope is negative and unstable otherwise. One can see that there is an interval of the mode power Q where two stable nonlinear localized modes of different shape and frequency can coexist. As we show in Ref. 5 this *bistability phenomenon* occurs as a direct manifestation of the nonlocality of the effective (linear and nonlinear) interaction between the defect rods which form the waveguide.

Acknowledgments

This work has been partially supported by the Large Grant Scheme of the Australian Research Council, the Australian Photonic Cooperative Research Centre, and the Planning and Performance Fund of the Institute of Advanced Studies.

References

1. J.D. Joannopoulos, R.D. Meade, and J.N. Winn, Photonic Crystals: Molding the Flow of Light (Princeton University Press, Princeton, 1995).
2. A. Blanco *et al.*, "Large-scale synthesis of a silicon photonic crystal with a complete three-dimensional bandgap near 1.5 micrometers," Nature **405**, 437-40 (2000).
3. M. Tokushima, H. Kosaka, A. Tomita, and H. Yamada, "Lightwave propagation through a 120° sharply bent single-line-defect photonic crystal waveguide," Appl. Phys. Lett. **76**, 952-4 (2000).
4. N.G.R. Broderick *et al.*, "Hexagonally poled lithium niobate: a two-dimensional nonlinear photonic crystal," Phys. Rev. Lett. **84**, 4345-8 (2000).
5. S.F. Mingaleev, Yu.S. Kivshar, and R.A. Sammut, "Long-range interaction and nonlinear localized modes in photonic crystal waveguides," Phys. Rev. E **62**, (4), 5777-82 (October 2000).

Propagating Fields

Modulation Instability of Spatially Incoherent Light Beams and Pattern Formation in Incoherent Wave Systems

By Detlef Kip, Marin Soljacic, Mordechai Segev, Evgenia Eugenieva, and Demetrios N. Christodoulides

Modulation instability (MI) is a universal process that appears in most nonlinear wave systems in nature. Because of MI, small amplitude and phase perturbations (from noise) grow rapidly under the combined effects of nonlinearity and diffraction (or dispersion, in the temporal domain). As a result, a broad optical beam (or a quasi-cw pulse) disintegrates during propagation, leading to filamentation or to break up into pulse trains. MI is generally considered as a precursor to solitons, because the filaments (or pulse trains) that emerge from the MI process are actually trains of almost ideal solitons. Over the years, MI has been systematically investigated in connection with numerous nonlinear processes. Yet, it was always believed that MI is inherently a coherent process and thus can appear only in nonlinear systems with a perfect degree of coherence. Earlier this year, however, we theoretically demonstrated[1] that MI can also exist in relation with partially incoherent wave packets or beams.

MI in nonlinear incoherent environments reveals several new features that have no counterpart in coherent wave systems. The most important new features are as follows. (1) The existence of a sharp threshold for nonlinear index change, below which perturbations (noise) on top of a uniform input beam decay and above which a quasi-periodic pattern forms. (2) The threshold depends on the coherence properties of the input beam: the threshold increases with decreasing correlation distance (decreasing spatial coherence). The intuition behind these features and the fundamental difference between MI in coherent and in incoherent wave systems can be understood in the following manner. A small periodic perturbation on a coherent beam remains periodic and maintains its modulation depth during linear diffraction. Thus, any self-focusing nonlinearity, no matter how small, increases the modulation depth and leads to instability, which is why coherent MI has no threshold. On the other hand, a perturbation on an incoherent beam diminishes its modulation depth during linear diffraction. The nonlinearity has to overcome this washout effect to gain instability, which is why incoherent MI has a threshold: it occurs only if the nonlinearity is strong enough to overcome the diffusive washout caused by diffraction. Furthermore, the more incoherent the beam, the higher the MI threshold.

Recently, we made the first experimental observation of incoherent MI.[2] We showed that, in a nonlinear partially coherent system (a nonlinear system of weakly correlated particles), patterns can form spontaneously (from noise) when the nonlinearity exceeds the threshold, and a periodic train of one-dimensional filaments

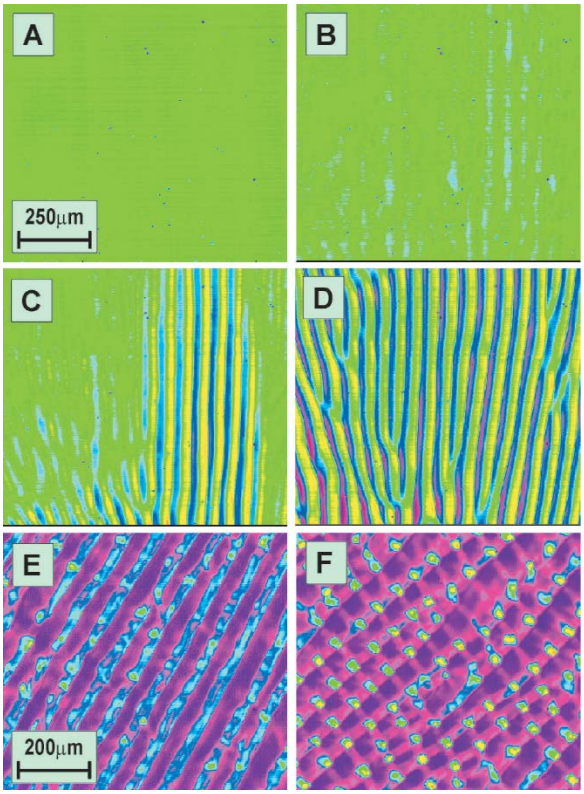

Modulation Instability Figure 1. Intensity structure of a partially spatially incoherent beam at the output plane of a nonlinear photorefractive crystal. The sample is illuminated homogeneously with a partial spatially incoherent light with a coherence length of l_c = 17.5 μm. The displayed area is (a)-(d) 1.0 mm x 1.0 mm, (e) and (f) 0.8 mm x 0.8 mm. The size of the nonlinear refractive-index change of the crystal increases successively from (a) $\Delta n_0 = 0$ (the linear case) to (b) 3.5×10^{-4}, (c) 4.0×10^{-4}, (d) 4.5×10^{-4}, (e) 9×10^{-4}, (f) 1×10^{-3}. The plots in (b)-(d) show the cases just below threshold (no features), at threshold (partial features), and just above threshold (features everywhere) for one-dimensional incoherent MI that leads to one-dimensional filaments. Far above this threshold, at a much higher value of the nonlinearity, the one-dimensional filaments become unstable (e), and finally become ordered in a regular two-dimensional pattern (f).

emerges. At a higher value of nonlinearity, the incoherent one-dimensional filaments display a two-dimensional instability and break up into self-ordered arrays of light spots. A typical experimental result is shown in Fig. 1. We emphasize that, in all the pictures displayed in Fig. 1, the correlation distance is much shorter than the distance between two adjacent stripes or filaments.

The ability to suppress MI has led to new families of solitons that have no counterpart whatsoever in the coherent regime. For example, it facilitated the observation of antidark solitons:[3] brightlike solitons superimposed on a uniform background. Such an entity was generally considered highly unstable and, to the best of our knowledge, has never been observed before.[4] Another example is the generation of stable (in the absolute sense) (1+1)-dimensional bright solitons in bulk Kerr media.[5] Again, an entity that has been considered highly unstable since 1974.

The discovery of incoherent MI actually reflects on many other nonlinear systems beyond optics: it implies that patterns can form spontaneously (from noise) in nonlinear many-body systems that involve weakly correlated particles, such as, for example, atomic gases at temperatures near the Bose-Einstein condensation (BEC) temperatures,[6] electrons in semiconductors at the vicinity of the quantum Hall regime, high-Tc superconductors. We believe and hope that, as has happened so many times in science, the best is yet to come.

Acknowledgments

This research is part of the Multi-University Research Initiative program on optical spatial solitons and is supported by the U.S. Army Research Office, the National Science Foundation, the Air Force Office of Scientific Research, the Israel Science Foundation, and the Israel Ministry of Science.

References

1. M. Soljacic, M. Segev, T. Coskun, D. N. Christodoulides, and A. Vishwanath, "Modulation instability of incoherent beams in noninstantaneous nonlinear media," Phys. Rev. Lett. **84**, 467 (2000).
2. D. Kip, M. Soljacic, M. Segev, E. Eugenieva, and D. N. Christodoulides, "Modulation instability and pattern formation in spatially incoherent light beams," Science **20,** 495-8 (2000).
3. T. Coskun, D. N. Christodoulides, Y. Kim, Z. Chen, M. Soljacic and M. Segev, "Bright spatial solitons on a partially incoherent background," Phys. Rev. Lett. **84**, 2374-77 (2000).
4. Y. S. Kivshar, "Nonlinear dynamics near the zero dispersion point in optical fibers," Phys. Rev. A **43**, 1677-9 (1991); N. Akhmediev and A. Ankiewicz, "Partially coherent solitons on finite background," Phys. Rev. Lett. **82**, 2661-4 (1999).
5. C. Anastassiou, M. Soljacic, M. Segev, D. Kip, E. Eugenieva, D. N. Christodoulides and Z. H. Musslimani, "Eliminating the transverse instabilities of Kerr solitons," Phys. Rev. Lett., to be published, December 2000.
6. See, e.g., Th. Busch and J. R. Anglin, "Motion of dark solitons in trapped Bose-Einstein Condensates," Phys. Rev. Lett. **84**, 2298-301 (2000).

Generation of Optical Spatiotemporal Solitons

By Xiang Liu, Kale Beckwitt, and Frank Wise

Students in undergraduate physics courses learn that beams of light spread out as they propagate, as a result of diffraction. Similarly, pulses of light spread in time as they propagate, as a consequence of group-velocity dispersion. Both effects occur in linear propagation. Any nonlinear effects generally cause a pulse or beam to decay even faster. However, under special conditions nonlinearity can be used to compensate the effects of diffraction or dispersion. Self-focusing can counter diffraction, or phase modulation can balance dispersion. The resulting field that propagates without spreading out is known as a soliton.

Temporal solitons in optical fibers are extensively studied and have begun to affect telecommunication systems. Spatial solitons, beams that propagate without spreading, have been observed in several different media in the last decade. Until last year, however, no one succeeded in generating pulses of light that are simultaneously solitons in time and space. The expression *light bullets* conveys the image of particle-like propagation that is achieved by such solitons.

Liu *et al.* recently reported what are to the best of our knowledge the first experimental observations of spatiotemporal solitons.[1,2] For these experiments they used quadratic nonlinear media such as barium metaborate. Second-harmonic generation under phase-mismatched

conditions produces a self-focusing nonlinearity that saturates at high intensities. In initial experiments a beam that overcomes diffraction in only one of the two transverse dimensions was produced, so the beam is in the form of a stripe. The temporal and spatial profiles of the soliton are shown in Fig. 1. The characteristic propagation length over which diffraction (dispersion) would cause the beam (pulse) to broaden is 5 mm. The data show that for propagation over five characteristic lengths (25 mm), the beam size (pulse duration) is constant and ~50 μm (100 fs). If the propagation were linear, the beam would have broadened to 300 μm and the pulse duration to 500 fs owing to diffraction and dispersion, and the intensity would be 30 times smaller. These solitons are significantly different from the familiar solitons in fibers because they consist of two fields (the fundamental and harmonic frequencies) that couple and trap each other.

Interestingly, such a soliton is not always stable. Liu *et al.* found that under certain conditions the stripe spontaneously breaks into a series of filaments.[3] This process produces confinement in the remaining transverse dimension, so the filaments are fully confined light bullets. Liu and co-workers make solitons in time and one spatial dimension, and nature takes care of the other spatial dimension. The experiment currently cannot support the propagation of light bullets over long distances, so new experiments are planned to produce the three-dimensional light bullets directly. The generation of spatiotemporal solitons has been viewed as a holy grail in the field of nonlinear waves. They may be usable in experiments to produce strong interactions between light and matter and as ideal bits in information-processing systems.

Generation of Optical Spatiotemporal Solitions Figure 1. Measured temporal (left) and spatial (right) profiles of spatiotemporal solitons in barium metaborate. The 25 mm corresponds to five diffraction or dispersion lengths.
Figure 2. The photograph represents two-dimensional space-time solitons that consist of fundamental (red) and harmonic (blue) fields, mutually trapped in the form of a stripe. The white spots result from modulation instability and constitute fully confined solitons, the light bullets.

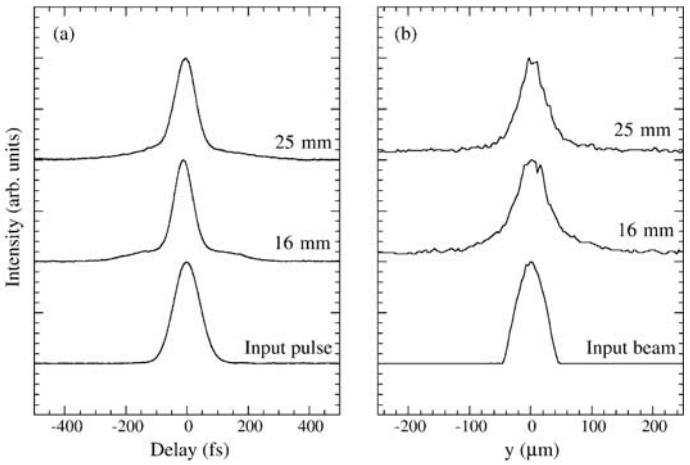

References

1. X. Liu, L. Qian, and F. W. Wise, "Generation of optical spatio-temporal solitons," Phys. Rev. Lett. **82**, 4631-4 (1999).
2. X. Liu, K. Beckwitt, and F. W. Wise, "Two-dimensional optical spatio-temporal solitons in quadratic media," Phys. Rev. E **62**, 1328-40 (2000).
3. X. Liu, K. Beckwitt, and F. W. Wise, "Transverse instability of spatio-temporal solitons in quadratic media," Phys. Rev. Lett. **85**, 1871-4 (2000).

Light Molecules: Dipole-Mode Vector Solitons

By Wieslaw Krolikowski, Barry Luther-Davies, Glen McCarthy, Matthias Geisser, Yuri Kivshar, Elena Ostrovskaya, Carsten Weilnau, Cornelia Denz, Juan J. García-Ripoll and Victor M. Pérez-García

One of the most important manifestations of optical nonlinearity, associated with an intensity-dependent refractive index, is spontaneous self-focusing of an optical beam that occurs because of lensing induced within the medium. When the strength of the focusing is such that it exactly balances diffraction, a bright optical spatial soliton forms, a self-trapped light beam that does not change its shape during propagation.[1] In a self-focusing medium in steady-state conditions, these bright solitons possess radial symmetry. However, any beam with a more complex geometry, such as one carrying angular momentum, decays into a number of bright spatial solitons (self-trapped bright filaments).

The idea to trap beams containing angular momentum (analogous to the spin of the beam) in structures of finite extent seems extremely attractive for the observation of spin-orbital interactions of light waves.[2] Trapping of a light wave carrying angular momentum may be performed with a soliton-induced waveguide created by a second optical beam propagating simultaneously through a self-focusing nonlinear medium. When the trapped beam is weak, linear guided wave theory can be applied, and therefore one can expect various types of (2 + 1)-dimensional composite solitons originating from trapping of different types of guided modes by the soliton-induced waveguide. Two examples of such lower-order structures were recently suggested in Refs. 2 and 3. The first type of vector soliton has a component with the doughnut structure of a

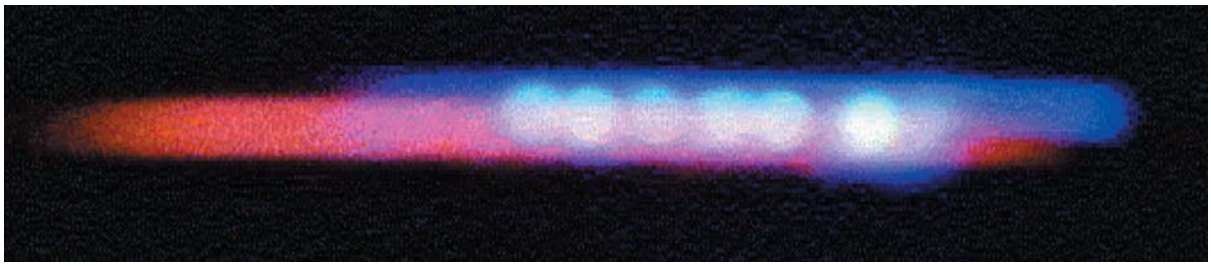

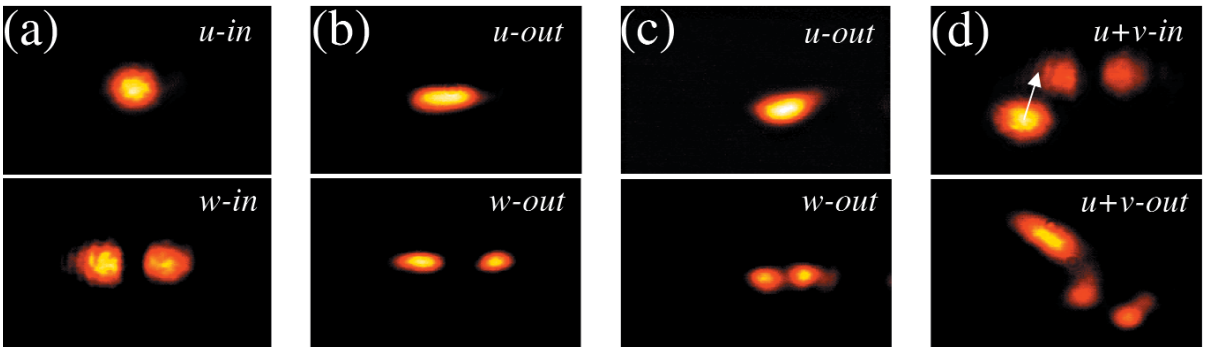

Dipole-Mode Vector Solitions Figure 1. Experimental demonstration of the formation of the dipole-mode soliton (a)-(c) as well as transformation of the linear-to-angular momentum in the collision event between a dipole-mode soliton and a scalar soliton, mutually coherent with the dipole component of the composite structure (d). The following are shown: (a) Input intensity of the fundamental (u) and dipole (w) components. (b) Output structure of dipole and fundamental beams after individual propagation in the nonlinear crystal. The dipole beam forms two separate solitons that repel because of the initial π-phase difference. (c) Output intensity distribution in both components of the dipole-mode vector soliton (molecule of light)—now the two repelling lobes of the dipole are trapped by the fundamental beam. (d) Intensity distribution of the dipole component (u) and the scalar beam (v) before (top) and after (bottom) the collision. The arrow indicates initial transverse velocity of the scalar soliton. Rotation of the dipole component after the interaction is clearly visible. The phase difference between the scalar soliton and the lobe of the dipole was approximately π.

Laguerre-Gaussian (LG_{01}) vortexlike mode and carries angular momentum.[2] The second type of vector soliton originates from trapping of a dipolelike Hermite-Gaussian (HG_{01}) mode by a soliton-induced waveguide.[3] It was recently shown[3] that, contrary to naïve intuition, a radially asymmetric dipole-mode soliton is more stable than a radially symmetric vortex-mode soliton, the latter undergoing a nontrivial symmetry-breaking instability and transforming into a rotating dipolelike structure that resembles two spiraling soliton beams. In fact, the dipole-mode soliton is a robust object that survives collisions with other localized structures, and it can be referred to as a *molecule of light*—a composite state of two simple beams, atoms of light.

Experimental observation of such dipole-mode vector solitons, molecules of light, was recently reported by Krolikowski *et al.*,[4] who used a photorefractive strontium barium niobate (SBN) crystal biased with a dc field of 1.5-2.5 kV to produce an effective saturable self-focusing nonlinearity. Krolikowski *et al.*[4] employed two different methods of producing the dipole component: phase imprinting and with a symmetry-breaking instability of a vortex-mode soliton. Observation of dipole-mode vector solitons in a SBN crystal was also reported by Carmon *et al.*[5]

More recently both theoretical and experimental results confirmed the robust nature of the dipole-mode solitons by observation of various scattering events of scalar spatial solitons and other dipoles on these molecules of light. Many amazing features of these unique objects have been revealed in the inelastic collision processes. These include the excitation of internal oscillatory modes of the molecules of light and the transformation of the linear momentum of an incident atom of light (scalar soliton) into the angular momentum of a dipole-mode soliton (see Fig. 1).

References and Notes

1. G. I. Stegeman and M. Segev, "Optical spatial solitons and their interactions: universality and diversity," Science, **286**, 1518-23 (1999).
2. Z. H. Musslimani, M. Segev, D. N. Christodoulides, and M. Soljacic, "Composite multihump vector solitons carrying topological charge," Phys. Rev. Lett. **84**, 1164-7 (2000).
3. J. J. García-Ripoll, V. M. Pérez-García, E.A. Ostrovskaya, and Yu. S. Kivshar, "Dipole-mode vector solitons," Phys. Rev. Lett. **85**, 82-5 (2000).
4. W. Krolikowski, E. A. Ostrovskaya, C. Weilnau, M. Geisser, G. McCarthy, Yu. S. Kivshar, C. Denz, and B. Luther-Davies, "Observation of dipole-mode vector solitons," Phys. Rev. Lett. **85**, 1424-7 (2000).
5. T. Carmon, C. Anastassiou, S. Lan, D. Kip, Z. H. Musslimani, M. Segev, and D. Christodoulides, "Observation of two-dimensional multimode solitons," Opt. Lett. **25**, 1113-1 5000).

New Member in the Family of Propagation-Invariant Optical Fields: Mathieu Beams

By Julio César Gutiérrez-Vega, Marcelo David Iturbe-Castillo, Eduardo Tepichin, Gustavo Ramírez, Ramon Martin Rodríguez-Dagnino and Savino Chávez-Cerda.

Propagation-invariant optical fields (PIOFs) generate interest because, under ideal conditions, they propagate indefinitely without changing their transverse intensity distribution. Their potential applications in wireless communications, optical interconnections, laser machining, and surgery make them highly useful. However, to create truly invariant optical fields, sources with infinite extent would be needed. Nevertheless, in the real world it is possible to create good approximations of such kinds of fields, and the distance over which they can propagate without significant alteration can range from several millimeters to tens of meters or more.

Beamlike approximations to PIOFs were first demonstrated by Durnin and co-workers,[1] who obtained transverse intensity ringed patterns with a J_0-Bessel profile and thus called them Bessel beams. Since that seminal study, research worldwide has followed by identifying the beams' many peculiar features. For some applications the ringed structure of Bessel beams can be a disadvantage. For this reason it is important to identify other three-dimensional propagating solutions of the wave equation with no ringed structure but with invariance.

Although there have been several related studies showing the possibility for creating PIOFs with different kinds of patterns, the studies have been based on the Cartesian and the circular solutions of the wave equa-

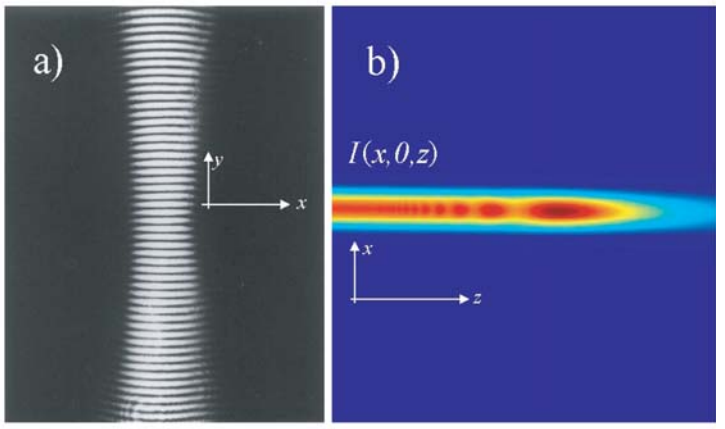

Mathieu Beams Figure 1. Fundamental Mathieu beam. (a) Experimental observation of the transverse intensity pattern of the zero-order Mathieu beam. (b) Simulation of the intensity evolution of a finite Mathieu beam; the panel shows the central part along the plane x-z.

tion.[2,3] In a recent paper, based on the McCutchen theorem,[4] Gutiérrez-Vega *et al.* demonstrated theoretically that in elliptic cylindrical coordinates it is possible to create PIOFs.[5] In that study the corresponding Hankel-Mathieu solutions of the Helmholtz equation were used to describe what we called Mathieu beams. Similar to plane waves and Bessel beams, the Mathieu beams also form an orthogonal and complete set in the sense that any propagation-invariant optical field can be represented as the superposition of Mathieu beams.[2,3]

Building on the theoretical research of Ref. 5, we have been able to produce approximations to the zero-order Mathieu beam experimentally. To create them, we identified the corresponding angular spectrum and observed that it can be approximated in the laboratory by an annular slit illuminated with a strip pattern with a Gaussian profile produced, for instance, with the help of a cylindrical lens.[5]

Fig. 1 shows the pattern obtained in the laboratory that propagated almost invariantly for up to 15 m. Fig. 1(a) shows the transverse pattern of the Mathieu beam, whereas Fig. 1(b) shows the simulation of the intensity evolution in the x-z plane corresponding to the central oval. It is important to note that at the sides of the pattern, although no light is apparent, field components that interfere destructively exist in that region. These field components are those that keep the pattern invariant in directions parallel to the x axis, as observed in Fig. 1(b). Our experimental results are in excellent agreement with the theoretical predictions. Also, our investigations show that it is possible to create propagation-invariant higher-order Mathieu beams with elliptic-ringed transverse patterns.

References

1. J. E. Durnin, J. J. Miceli, and J. H. Eberly, "Diffraction-free beams," Phys. Rev. Lett. **58**, 1499-501 (1987).
2. V. Kettunen and J. Turunen, "Propagation-invariant spot arrays," Opt. Lett. **15**, 1247-9 (1998).
3. R. Piestun and J. Shamir, "Generalized propagation-invariant wave fields," J. Opt. Soc. Am. A **15**, 3039-44 (1998).
4. G. Indebetouw, "Nondiffracting optical fields: some remarks on their analysis and synthesis," J. Opt. Soc. Am. A **6**, 150 (1989).
5. J. C. Gutiérrez-Vega, M. D. Iturbe-Castillo, and S. Chávez-Cerda, "Alternative analytic formulation for invariant optical fields: Mathieu beams," Opt. Lett. **25**, 1493-5 (2000).

Quantum Optics

Solitons in a Bose-Einstein Condensate

By David L. Feder

The recent observation of Bose-Einstein condensation (BEC) in weakly interacting gases[1] has opened the door to the field of coherent matter-wave optics. BEC occurs when a macroscopic number of particles obeying Bose statistics occupy a single quantum state. This coherent occupation of the ground state in the atomic trap is analogous to the many photons in the cavity of a single-mode laser. The weak (but nonnegligible) interactions between atoms, however, modify the structure of the occupied mode and introduce nonlinearity into the system.

When the many-atom state is treated within a mean-field approximation, a nonlinear term arises in the equations of motion for the condensate wave function. The resulting nonlinear Schrödinger equation is formally similar to that describing the propagation of light in

Solitons in a Bose-Einstein Condensate Figure 1. Experimental (A-E) and theoretical (F-J) images of the integrated condensate density for various times after the phase imprint. Because the imaging technique is destructive, each frame shows a different condensate.

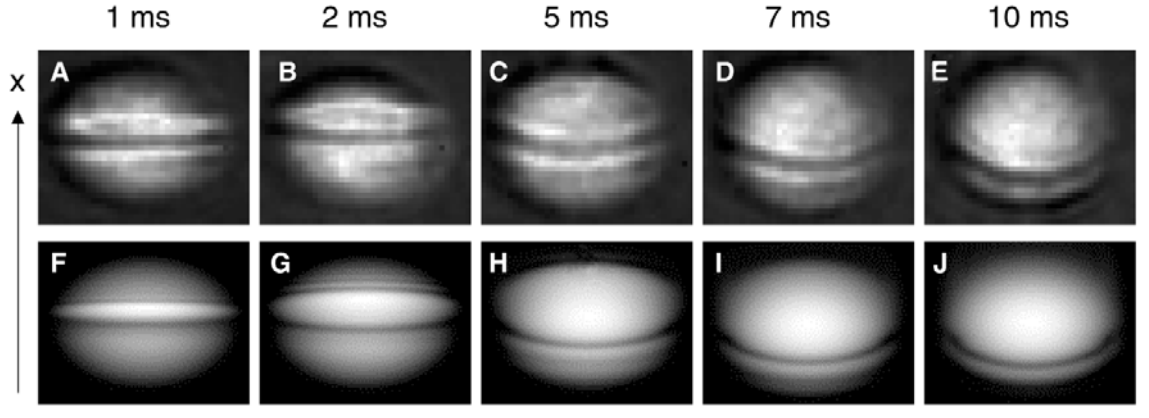

nonlinear media. Since ultracold gases ultimately may have applications in such areas as nanotechnology, precision metrology, and quantum computation, it is important that the nonlinear phenomena exhibited by these systems be understood. The new discipline of nonlinear atom optics was strikingly inaugurated in 1999 by the observations of four-wave mixing of matter waves.[2]

Groups based at the National Institute of Standards and Technology (NIST) in Gaithersburg, Maryland,[3] and at the Universität Hannover in Germany[4] recently reported another aspect of nonlinear atom optics: the observation of dark solitons in a BEC. Solitons are localized traveling waves that preserve their spatial profile because of a balance between the dispersion and nonlinearity. Condensates with repulsive interactions support dark solitons, which are notches in the wave-function amplitude and are characterized by a step in the phase. Exploiting the latter property, both research groups generated dark solitons by optically imprinting a localized step on the condensate phase. The atoms were exposed to a short pulse of laser light at a frequency far from atomic resonance, to make absorption of photons negligible. The energy associated with the atom-laser interaction (light shift) created an intensity-dependent phase of the condensate wave function. By illumination of only half the condensate, the phase step appropriate for generating solitons was imprinted onto the BEC. The phase distribution was subsequently measured at NIST by use of a novel matter-wave interferometer.

Images of the NIST condensate after the phase imprint, corresponding to both experimental data and numerical simulations, are shown in Fig. 1. The dark solitons appear as notches propagating downward, more slowly than the sound waves (phonons) that travel in the opposite direction. Since the speed is proportional to the atomic density, the solitons curve as they travel through the condensate. At longer times the solitons are found numerically to stop completely, then break up into the quantized vortices characteristic of a superfluid. The optical phase imprinting and matter-wave interferometry techniques employed in the study of dark solitons are new tools available for the manipulation and analysis of Bose-Einstein condensates. These may be extended to enable direct modification of the condensate amplitude, allowing for complete coherent control of these new states of matter.

References

1. F. Dalfovo, S. Giorgini, L. Pitaevskii, and S. Stringari, "Theory of Bose-Einstein condensation in trapped gases," Rev. Mod. Phys. **71**, 463-512 (1999).
2. L. Deng, E. W. Hagley, J. Wen, M. Trippenbach, Y. Band, P. S. Julienne, J. E. Simsarian, K. Helmerson, S. L. Rolston, and W. D. Phillips, "Four-wave mixing with matter waves," Nature **398**, 218-20 (1999).
3. J. Denschlag, J. E. Simsarian, D. L. Feder, C. W. Clark, L. A. Collins, J. Cubizolles, L. Deng, E. W. Hagley, K. Helmerson, W. P. Reinhardt, S. L. Rolston, B. I. Schneider, and W. D. Phillips, "Generating solitons by phase engineering of a Bose-Einstein condensate," Science **287**, 97-101 (2000).
4. S. Burger, K. Bongs, S. Dettmer, W. Ertmer, K. Sengstock, A. Sanpera, G. V. Shlyapnikov, and M. Lewenstein, "Dark solitons in Bose-Einstein condensate," Phys. Rev. Lett. **83**, 5198-201 (1999).

Quantum Switch

By Byoung S. Ham

Because of the rapid growth rate of the Internet, 15% per month, information communications traffic will reach several tens of terabits/s in a few years. To process such high-capacity information traffic without delay, ultra-high-speed optical switches are required. Recently, optical switching of near picosecond speed has been demonstrated in semiconductor quantum wells with intersubband transitions.[1] The optical switching time in Ref. 1, however, is absolutely limited by the population relaxation time T_1. Here I introduce an entirely different switching technique, so-called quantum switching, to overcome the T_1 limitation in the switching speed. The new optical switching technique is based on the simultaneous two-photon coherence exchange in a four-level system interacting with three-laser fields.[2] Ultrafast two-photon coherence swapping occurs when dark resonance[3] conditions are satisfied.

For the past 10 years many researchers have studied the basic physics of the dark resonance phenomenon by use of atomic gases, impurity-ion-doped crystals, and semiconductor quantum wells.[3] In a Λ-type three-level system, two resonant optical fields can excite coherence on the ground states by means of two-photon reso-

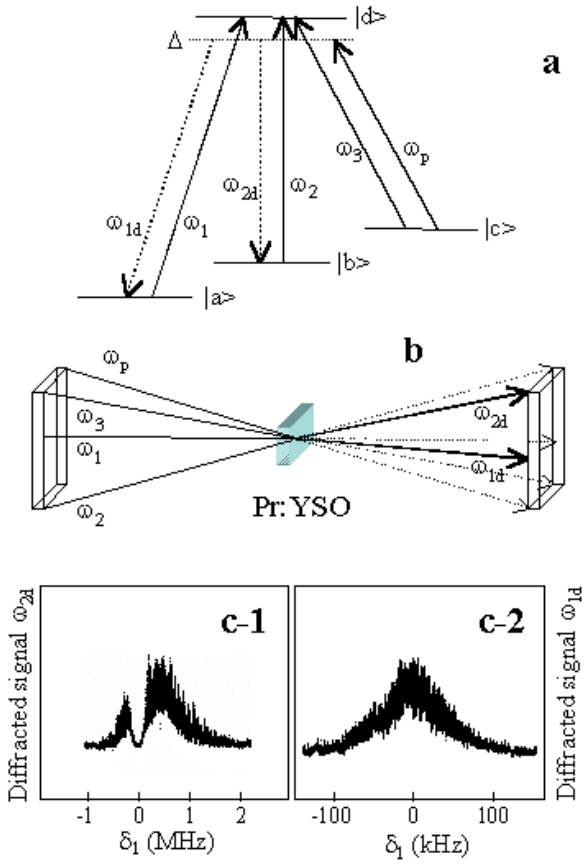

Quantum Switch Figure 1. (a) Energy schematic for quantum switching, (b) beam-propagation geometry, and (c) intensity of diffracted signals.

nance. One of the superposition states created by the matter-field interactions is decoupled from the excited state so that even optically thick media can be transparent to the resonant optical fields. This decoupled state is the origin of the dark resonance.

The dark resonance, however, shows different features in a four-level system. When three-resonant laser fields (ω_1, ω_2, and ω_3) are applied to the four-level system [see Fig. 1(a)], one of the coherences excited on the three-ground states can be suppressed while the others are enhanced.[2] In Fig. 1(b) the coherent phase gratings can be formed by noncopropagating laser fields ω_1, ω_3 and ω_2, ω_3 on the transitions $|a\rangle$-$|c\rangle$ and $|b\rangle$-$|c\rangle$, respectively. The phase gratings are then detected by nondegenerate four-wave mixing processes satisfying the phase-matching conditions of $k_{1d} = k_1 - k_3 + k_P$ and $k_{2d}=k_2 - k_3 + k_P$, respectively. Here k_{id} (i=1.2) is a propagation vector of the beam ω_{id}. The four-wave mixing signal intensities of $I_{1d}(\omega_{1d})$ and $I_{2d}(\omega_{2d})$ are proportional to the square of the coherence strength $[\mathrm{Re}(\rho_{ac})]^2$ and $[\mathrm{Re}(\rho_{bc})]$,[2] respectively.[4] The dark-resonance-induced two-photon coherence was experimentally demonstrated in a three-level system for efficient excitation that was built up faster than the population relaxation time T_1.[5] This implies that the quantum switching should be used for subpicosecond optical switches.

Fig.s 1(c-1) and 1(c-2) show experimental demonstrations in Pr:YSO with a cw laser. The signal intensity $I_{2d}(\omega_{2d})$ becomes substantially suppressed as the detuning δ_1 ($\omega_{da} - \omega_1$) comes close to zero, whereas the signal intensity $I_{1d}(\omega_{1d})$ is greatly enhanced ($\omega_{db} - \omega_2 = 10$ kHz; $\Delta = 1.5$ MHz). This signal enhancement of $I_{1d}(\omega_{1d})$ and the suppression of $I_{2d}(\omega_{2d})$ at $\delta_1 = 0$ are due to the dark resonance changes in the hyperfine states $|a\rangle$-$|c\rangle$ and $|b\rangle$-$|c\rangle$, respectively. The suppressed spectral width of $I_{2d}(\omega_{2d})$ at $\delta_1 = 0$ is narrower than the laser jitter, and it is an experimental proof that the four-wave mixing generation is based on the dark resonance. Therefore the swap of the diffraction signals' intensity at $\delta_1 = 0$ is due to the perturbation of the dark states when all three beams are (near) resonant to the system.[2]

References

1. A. Neogi, T. Mozume, H. Yoshida, and O. Wada, "Intersubband transitions at 1.3 and 1.55 μm in a novel coupled InGaAs-AlAsSb double-quantum-well structures," IEEE Photonics Technol. Lett. **11**, 632-4 (1999).
2. B. S. Ham and P. R. Hemmer, "Coherence switching in a four-level system: quantum switching," Phys. Rev. Lett. **84**, 4080-3 (2000).
3. S. E. Harris, "Electromagnetically induced transparency," Phys. Today **50** (7), **36** (1997); B. S. Ham, M. S. Shahriar, and P. R. Hemmer, "Enhanced nondegenerate four-wave mixing owing to electromagnetically induced transparency in a spectral hole-burning crystal," Opt. Lett. **22**, 1138-40 (1997); G. B. Serapiglia, E. Paspalakis, C. Sirtori, K. L. Vodopyanov, and C. C. Philips, "Laser-induced quantum coherence in a semiconductor quantum well," Phys. Rev. Lett. **84**, 1019-22 (2000), and references therein.
4. B. S. Ham, M. S. Shahriar, and P. R. Hemmer, "Efficient phase conjugation via two-photon coherence in an optically dense crystal," Phys. Rev. A. **59**, R2583-6 (1999).
5. B. S. Ham, M. S. Shahriar, M. K. Kim, and P. R. Hemmer, "Spin coherence excitation and rephasing with optically shelved atom," Phys. Rev. B **58**, R11825-8 (1998).

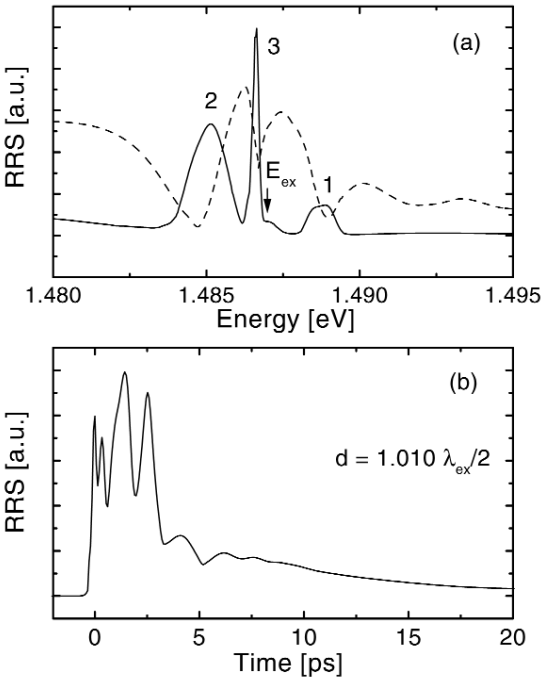

Quantum Wells Figure 1. (a) Measured RRS spectra (solid curve) using a spectral interferometric technique and corresponding reflection (dashed curve) from an $N = 100$ multiple QW for a QW periodicity $d = 1.010\ \lambda_{ex}/2$. (b) Corresponding RRS time dynamics. Note that the first peak is due to surface scattering of the pump pulse.

Quantum Wells Coupled by Light: Eigenmode Dynamics in Resonant Rayleigh Scattering

By Claudia Ell, Bernhard Grote, Galina Khitrova, Hyatt M. Gibbs, Stephan W. Koch, John P. Prineas, and Jagdeep Shah

Whereas semiconductor quantum wells (QWs) spaced close together can be coupled electronically, QWs with arbitrary periodicity can be coupled by light. If the 1-s exciton resonance is light-coupled in N QWs, N eigenmodes for the collective structure result, each mode with an oscillator strength, energy, and radiative lifetime that depends on the QW periodicity. A light pulse resonant with the exciton resonance scatters not simply off the exciton resonance but off several resonances associated with the eigenmodes. Depending on the periodicity, emission can be suppressed or enhanced.[1] Coherent light emitted in directions different from that of the excitation and reflected beams, generally called secondary emission, consists of resonant Rayleigh scattered light (RRS) arising from an interplay between disorder and light-coupling effects in the low-excitation regime.

Since the discrete arrangement of N QWs does not have the continuous translational invariance of a bulk semiconductor, the polariton modes in a bulk medium are replaced with the N eigenmodes of the discrete structure. Disorder breaks the translational invariance in the QW plane, thus relaxing the momentum conser-

vation that prevents exciton decay in secondary directions and allowing for a coherent RRS emission into nonspecular directions. Until recently, RRS from a multiple-QW system was believed to give solely information about the underlying disorder.[2] However, the RRS signal can carry the imprint of the emission environment rather than just information about disorder.[3,4]

Study of the RRS from an $N = 100$ QW sample showed that at Bragg periodicity ($d = \lambda_{ex}/2$), where all eigenmodes are optically inactive except the superradiant mode, RRS is strongly suppressed. The N-times-enhanced decay rate of the superradiant mode compared with a single QW forces the reemission of the polarization in the excitation and reflected directions before RRS can build up. For larger periodicities other modes become optically active and appear as distinct peaks in the RRS spectrum, each characterized by its own radiative width [see Fig. 1 (a)]. Only a few modes have significant oscillator strength to be observed simultaneously at a given periodicity, because the coupling strength of a specific mode varies with the periodicity. The corresponding time signal reveals a complex beating behavior [see Fig. 1 (b)] predominantly between modes 1 and 2 at earlier times and between the longer living modes 1 and 3 at later times. It also shows the strong dependence of both the characteristic rise and decay times of the RRS signal on the radiative decay rates of the contributing modes. The peaks in the RRS spectra match the dips in measured reflection spectra, which are related to individual eigenmodes, thus further demonstrating the dominance of the light-coupling effects in secondary emission. A recently developed theory,[3] in which the microscopic material equations describing the excitons in disordered QWs are coupled self-consistently to the optical field, reproduces the experimental findings qualitatively well.

Acknowledgments

The Tucson group acknowledges support by the National Science Foundation Atomic, Molecular, Optical, and Plasma Physics Joint Services Optics Program (Air Force Office of Scientific Research and Army Research Office), and the Humboldt Research Program (H. M. Gibbs). The Marburg group thanks the Max-Planck Research program, the Deutsche Forschungsgemeinschaft, and the Leibniz program.

References

1. M. Hübner, J. P. Prineas, C. Ell, P. Brick, E. S. Lee, G. Khitrova, H. M. Gibbs, and S. W. Koch, "Optical lattices achieved by excitons in periodic quantum well structures," Phys. Rev. Lett. **83**, 2841-4 (1999).
2. V. Savona, S. Haacke, and B. Deveaud, "Optical signatures of energy-level statistics in a disordered quantum system," Phys. Rev. Lett. **84**, 183-6 (2000).
3. J. P. Prineas, J. Shah, B. Grote, C. Ell, G. Khitrova, H. M. Gibbs, and S. W. Koch, "Dominance of radiative coupling over disorder in resonance Rayleigh scattering in semiconductor multiple quantum-well structures," Phys. Rev. Lett. **85**, 3041-4 (2000).
4. G. Malpuech, A. Kavokin, W. Langbein, and J. M. Hvam, "Resonant Rayleigh scattering of exciton-polaritons in multiple quantum wells," Phys. Rev. Lett. **85**, 650-3 (2000).

Spectral Imaging

Reconstruction of Fiber Gratings by Use Of Time-Frequency Signal Analysis: Application to Distributed Sensing

By José Azaña and Miguel A. Muriel

Fiber gratings (FGs) have evolved into critical components for a multitude of applications in all-fiber-optic communication systems. The problem of synthesizing or reconstructing a FG structure (grating period and/or index modulation) from its corresponding reflection response is extremely important with regard to device design and has attracted considerable research interest.[1]

Recently we developed a technique for reconstructing the grating period of an arbitrary FG structure (including the length of the structure) from its corresponding complex reflection.[2, 3] Our technique is based

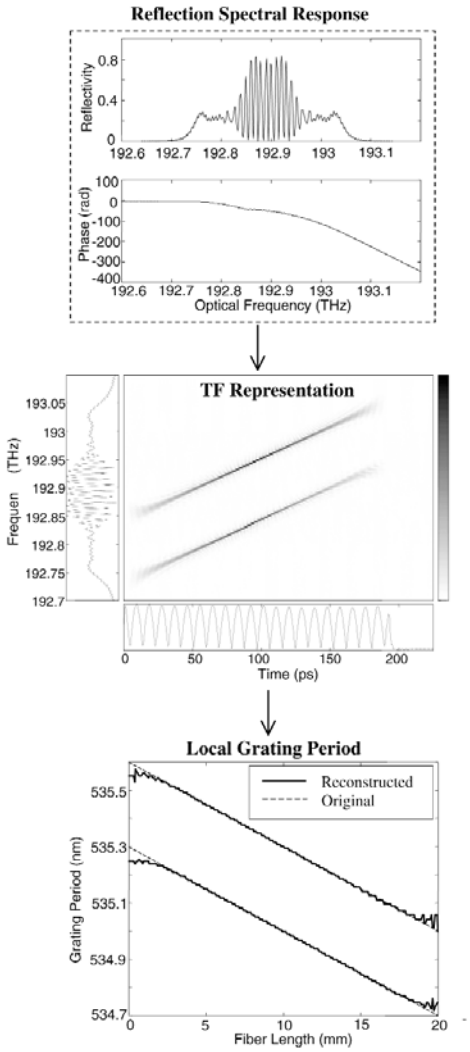

Reconstruction of Fiber Gratings Figure 1. Block diagram of the proposed technique for reconstruction of the local grating period in FG structures from the reflection response. The example shows the process and the results for a chirped moiré FG.

on a joint time-frequency (TF) signal analysis.[4] Fig. 1 is a schematic diagram of the proposed synthesis process. In the example, the technique is applied to a chirped moiré FG (superimposed chirped FGs). We begin with the complex reflection coefficient of the FG structure. The TF representation of this reflection response provides key and new information about the corresponding physical structure. An adequate treatment of this information permits the reconstruction of the grating period variation along the FG length. The reconstruction technique requires a TF representation with simultaneous high-joint TF resolution and reduced interference effects. The required representation can be obtained by a suitable combination of the high-resolution Wigner-Ville (WV) distribution and the cross-terms-free spectrogram (SP).[4] Fig. 1 shows the optimal TF distribution of the field reflection coefficient. By calculating the average frequency for each two-dimensional distribution, we obtained the associated one-dimensional TF plot. From this result we can then estimate the grating period variation along the fiber length by use of two scale changes: the time-to-fiber length uses the basic relation between the round-trip propagation time and the fiber distance measured from the device input; the frequency-to-grating period is given by the Bragg condition.

We note that, although the TF technique is limited in the sense that it can recover information only about the grating period and length, these are nevertheless important grating parameters in the synthesis process. This is especially true for FGs used in distributed sensing applications in which applied strain or temperature profiles can cause significant nonuniform variations to the grating period. In this respect, we recently showed that the TF synthesis technique can also be applied to recover arbitrary distributions of axial strain (or temperature) along a FG from its reflection response.[5] We have demonstrated that this new technique permits accurate strain reconstruction and overcomes the main limitations present in the techniques previously reported for the same purpose. In general and in view of our results, we conclude that the TF methods can be considered powerful and general tools for the design of FGs for different applications, i.e., for the choice of a parameter set that governs FG behavior. And one should bear in mind that the availability of general tools for analysis and characterization of grating structures becomes much more important as the FG writing techniques permit the fabrication of more complex structures.

References

1. See, for example, R. Feced, M. N. Zervas, and M. A. Muriel, "An efficient inverse scattering algorithm for the design of nonuniform fiber Bragg gratings," IEEE J. Quantum Electron. **35**, 1105-15 (1999), and references therein.
2. M. A. Muriel, J. Azaña, and A. Carballar, "Fiber grating synthesis by use of time-frequency representations," Opt. Lett. **23**, 1526-8 (1998).
3. J. Azaña and M. A. Muriel, "Reconstruction of fiber gratings period profile by employing Wigner-Ville distributions and spectrograms," J. Opt. Soc. of Am. A **17** 2496-505 (December 2000).
4. L. Cohen, Time-Frequency Analysis (Prentice-Hall, Englewood Cliffs, N. J., 1995).
5. J. Azaña and M. A. Muriel, "Reconstructing arbitrary strain distributions within fiber gratings by time-frequency signal analysis," Opt. Lett. **24**, 698-700 (2000).

Diffraction Resolution Barrier Fundamentally Broken in Far-Field Fluorescence Microscopy

By Stefan W. Hell and Thomas A. Klar

It is commonly assumed that the extent of the focal spot of a lens is not reducible beyond the wavelength of light λ, because diffraction demands an extent of at least λ/3 in the focal plane and λ along the optic axis. As a consequence, for more than a century focused light was abandoned whenever higher spatial definitions were required. In microscopy Abbe's diffraction resolution limit has been paradigmatic. Consequently, electron, atomic force, X-ray, and near-field optical microscopes have been invented, but these great instruments fail at visualizing the interior of live cells. Hence far-field light microscopy and particularly fluorescence microscopy have remained of utmost importance in biological research. By detecting fluorescent proteins and tagged cellular organelles, (confocal) fluorescence microscopes visualize life at the micrometer scale but with a resolution limited by diffraction.

On the basis of the proposal of stimulated emission depletion (STED) microscopy,[1] the diffraction barrier has now been broken in a fundamental way.[2] Compared with confocal microscopy, with STED microscopy nearly spherical fluorescence spots were generated that are twice as narrow in the focal plane and 5 times sharper along the optic axis (see Fig. 1). The resulting spot vol-

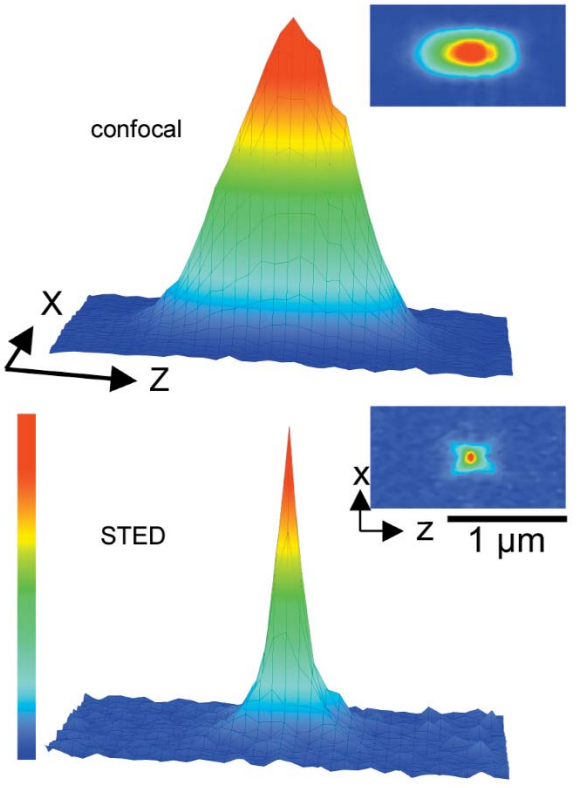

Diffraction Resolution Barrier Figure 1. Broken diffraction barrier in fluorescence microscopy: Diffraction-limited fluorescence spot of a confocal microscope (top) is squeezed by stimulated emission to subdiffraction dimensions, 90-110-nm FWHM in the lateral and the axial directions (bottom).

ume of 670 zeptoliters (1 zl = 10^{-21} l) is 18 times smaller than in the confocal counterpart and is the smallest fluorescent spot ever created with focused light.

The basic idea of STED microscopy is to quench the excited fluorophores nondestructively at the rim of the excitation focal spot through stimulated emission. For this purpose two synchronized trains of ultrafast laser pulses are employed: A visible excitation pulse is followed by a red-shifted STED counterpart. The wavelength of the quenching STED pulse was adjusted in the red edge of the emission spectrum.[2] The STED pulse forces the excited molecules at the focal rim to a vibrational level of the ground state from which they relax further by vibrational relaxation. To stop fluorescence at the focal rim only, the STED beam was shaped in a doughnut fashion so that fluorescence from the focal center was spared. Application of the STED-fluorescence microscope yielded the first far-field images with subdiffraction resolution.[2] Images of live yeast cells and E. coli bacteria revealed details not attainable with the confocal microscope. STED has also proven key to mapping the lifetime of the excited state of fluorophores in a cell from the nanosecond down to the femtosecond scale.[3] Besides providing subdiffraction imaging, STED may also enable local restriction of chemical reactions, such as those occurring in photoinduced three-dimensional data storage, to a spatial volume hitherto inconceivable with focused light.

References

1. S. W. Hell and J. Wichmann, "Breaking the diffraction resolution limit by stimulated emission: stimulated emission depletion microscopy," Opt. Lett. **19**, 780-2 (1994).
2. T. A. Klar, S. Jakobs, M. Dyba, A. Egner, and S. W. Hell, "Fluorescence microscopy with diffraction resolution limit broken by stimulated emission," Proc. Natl. Acad. Sci. USA **97**, 8206-10 (2000).
3. M. Dyba, T. A. Klar, S. Jakobs, and S. W. Hell, "Ultrafast dynamics microscopy," Appl. Phys. Lett. **77**, 597-9 (2000).

Metal Nanoparticles for Spectrally Coded Optical Data Storage

By Harald Ditlbacher, Joachim Rudolf Krenn, Bernhard Lamprecht, Alfred Leitner, and Franz Rembert Aussenegg

Particle plasmons in metal nanoparticles open up a new method of optical data storage by means of spectral coding by particles with different resonance wavelengths. Metal nanoparticles (e.g., from silver or gold) are deposited upon a transparent substrate. The particle plasmon is driven by an evanescent field obtained by total internal reflection. From the scattering intensity detected with the conventional optical far-field technique, one can determine whether a particle is in resonance at the irradiated wavelength. As for a given polarization state, the resonance wavelength of a particle can be determined by its axes ratio. A spectrally coded data storage by means of plasmon resonances can be obtained by appropriately shaped designs and particle orientation.

The metal particles that we used range from 30 to 150 nm. This size allows the arrangement of several differently shaped and oriented particles on a sample spot with a diameter that corresponds to the typical resolution limit of an optical microscope (approximately 500 nm), which is also the area typically occupied by a pit on a conventional compact disk (CD pit). The scattered light that emerges from that spot has a spectral composition determined by the different resonance wavelengths given by the different shapes and orientations of the particles contained in the spot. Thus, the storage of additional information in the area occupied by a conventional optical storage element (CD pit) is possible if one deposits a group of several individually shaped nanoparticles.

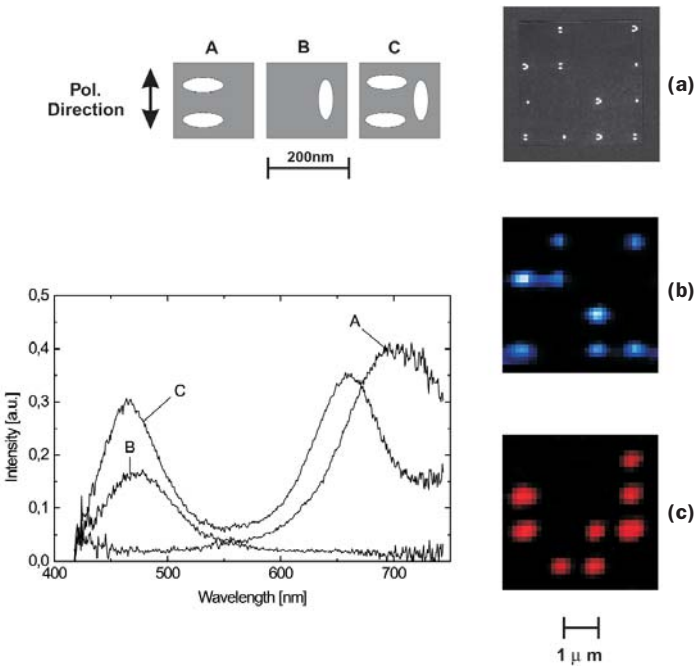

Metal Nanoparticles Figure 1. Letters A, B, and C represent metal nanoparticles that correspond to scattering spectra. (a), Pictures of a sequence of different letters on a substrate taken with a scanning electron microscope. Scattering under blue, (b), and red, (c), irradiation of light.

For the physical storage elements of the spectrally coded information, we chose three different arrangements of metal nanoparticles that correspond to three different letters, designated as A, B, and C in Fig. 1. Each arrangement consists of a different number of various orientations of elongated metal nanoparticles. For the chosen geometry and polarization direction (normal to the plane of incidence) of the irradiated light, two particle resonances can be excited, corresponding to the two axes that are parallel to the substrate plane.[1]

From the scattering spectra in Fig. 1 one can recognize that, for the given polarization direction of irradiated light, the letter A scatters light only in the red (around 680 nm), B scatters light only in the blue (around 480 nm), but the letter C scatters light in both spectral regions.

To achieve a practical realization, we covered a substrate surface with the letters A, B, and C in random sequence.[2] A scanning electron microscope sample image is shown in Fig. 1a. Figs. 1b and 1c show the scattering images of the sample section shown in Fig. 1a,

which was obtained by irradiation of blue (488 nm in Fig. 1b) and red (633 nm in Fig. 1c) laser light. The letter A is visible only under red light illumination, B only under blue light illumination, and C is visible under both red and blue light. For the sake of visual clarity the distance between individual letters was chosen to be somewhat larger (1.5 μm) than necessary (0.5 μm). The space on a data point is large enough to carry a letter consisting of considerably more metal particles than what is shown here. This enables correspondingly more separable scattering wavelengths and thus a higher storage density.

References

1. W. Gotschy, K. Vonmetz, A. Leitner, and F. R. Aussenegg, "Optical dichroism of lithographically designed silver nanoparticle films," Opt. Lett. **21**, 1099-101 (1996).
2. H. Ditlbacher, J.R. Krenn, B. Lamprecht, A. Leitner, F.R. Aussenegg, "Spectrally coded optical data storage by metal nanoparticles," Opt. Lett. **25**, 563-5 (2000).

SPECTROSCOPY

Remote Measurements of Volcanic Gases With a Diode-Laser-Based Spectrometer

By Livio Gianfrani and Paolo De Natale

Gaseous emissions of volcanoes can be regarded as telegrams from the Earth's interior, providing direct information on the nature of magma.[1] Temporal variations in the chemical composition and flux of volcanic gases can be predictors of volcanic eruptions. For this reason volcanic emissions are regularly monitored. In particular, gas samples are periodically collected and analyzed, mainly by use of gas-chromatographic techniques. Nevertheless, *in situ* sampling is often impractical and hazardous. Morever, *in situ* monitoring is not suited for every kind of device, a volcanic site being a hostile environment, because of the simultaneous presence of corrosive compounds, high temperatures, and, often, various kinds of particles and smoke. Surely, remote techniques would represent a safer and more appropriate alternative.

Recently, optical instruments have shown great potential for remote monitoring of volcanoes. Indeed, Fourier transform infrared spectroscopy,[2] as well as lidar techniques,[3] have been successfully tested in many field campaigns. More recently, we have demonstrated remote monitoring of a fumarolic gas flow, using a diode-laser-based absorption spectrometer,[4] which allows for real-time and simultaneous monitoring of more molecular species. We use distributed-feedback (DFB) semiconductor diode lasers as coherent sources and telecommunication optical fibers, which allow us to leave the entire setup in a safe place, far from the emissions. The spectrometer was tested at Solfatara, a volcano near Naples. Two lasers, tuned to the 1.393-μm vibrational band of H_2O and to the 1.578-μm band of CO_2, respectively, are launched into a single-mode fiber (see Fig. 1) that ends on the fumarolic flow. Here the output-collimated radiation passes through a specially designed glass cell, in which the volcanic gas flows. Then the bichromatic beam is focused into a multimode fiber that returns the beam to the bench. A dichroic filter splits such a beam into two parts, each focused on a detector. Simple absorption spectroscopy is performed through periodic scans of the laser frequencies over the H_2O and the CO_2 lines. Gas concentrations are retrieved from absorption spectra, by use of the Beer-Lambert law, with a relative uncertainty of ~3% for H_2O and ~15% for CO_2. The sensitivity, as well as the accuracy, for CO_2 detection can be improved by ~2 orders of magnitude, by use of a 2-μm-wavelength DFB diode laser. Research is in progress in this direction.

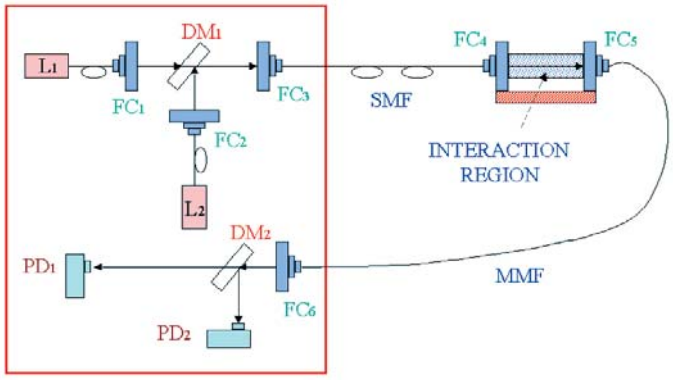

Remote Measurements of Volcanic Gases Figure 1. Sketch of the spectrometer, taken from Reference 4. L1 and L2, diode laser sources; FC, input-output fiber ports; DM, dichroic mirror; PD, photodetector; SMF and MMF, single-mode and multimode fibers, respectively.

It is worth noting that our spectrometer can continuously operate for long periods of time when powered with batteries and solar panels. This is an interesting perspective that would enable the installation of a surveillance net in active volcanic areas, allowing for continuous acquisition of data. Therefore it would offer a concrete possibility to relate volcanic events to variations in contents of some molecular species.

Many other gases of interest can be monitored as well. In the case of gases present in trace amounts, more-sensitive detection techniques, such as two-tone frequency modulation spectroscopy, are required and can be implemented without affecting some important features of our spectrometer, such as the small dimensions and low power consumption.

References

1. K. Notsu, T. Mori, G. Igarashi, Y. Tohjima, and H. Wakita, "Infrared spectral radiometer: a new tool for remote measurement of SO_2 in a volcanic gas," Geochem. J. **27**, 361-6 (1993).
2. P. Francis, M. R. Burton, and C. Oppenheimer, "Remote measurements of volcanic gas compositions by solar occultation spectroscopy," Nature **396**, 567-70 (1998).
3. P. Weibring, H. Edner, S. Svanberg, G. Cecchi, L. Pantani, R. Ferrara, and T. Caltabiano, "Monitoring of volcanic sulphur dioxide emissions using differential absorption lidar (DIAL), differential optical absorption spectroscopy (DOAS), and correlation spectroscopy (COSPEC)," Appl. Phys. B **67**, 419-6 (1998).
4. L. Gianfrani, P. De Natale, and G. De Natale, "Remote sensing of volcanic gases with a DFB-laser-based fiber spectrometer," Appl. Phys. B **70**, 467-70 (2000).

ULTRAFAST TECHNOLOGY

Ultrafast All-Optical Switching Based on Inter-Subband Transition in GaN/AlGaN and InGaAs/AlAsSb Multiple Quantum Wells

By Osamu Wada, Haruhiko Yoshida, Teruo Mozume, Arup Neogi, Nikolai Gergiev, Tomoyuki Akiyama, Kiyoshi Asakawa, Nobuo Suzuki, Norio Iizuka, Kei Kaneko, Takashi Asano, and Susumu Noda

The intersubband transition (ISB-T) in semiconductor quantum wells (QWs) has the advantages of ultrafast relaxation time, a large transition dipole moment, and wide tunability of transition wavelength. ISB-T has been popular for use in optoelectronic devices such as cascade lasers,[1] photodetectors, and optical switches.[2] An all-optical switch is one of the critical devices for development of optical time-division multiplexed (OTDM) communication systems at a bit rate of 100 Gbits/s and beyond. The application of ISB-T is extremely attractive, because it can eliminate the effect of a slow carrier recombination lifetime (in nanoseconds), which restricts the operation speed of conventional semiconductor-based optoelectronic devices. For this application of the ISB-T, there is a prerequisite to demonstrate ultrafast switching times in the picosecond region as well as in the femtosecond region, and the operating wavelength in the telecommunication band including 1.55 μm.

In our research project on femtosecond technology [3] at the Femtosecond Technology Research Association (FESTA), important breakthroughs were recently demonstrated by the introduction of two different novel material systems: one is the demonstration of response time in the femtosecond region (150 fs) in GaN/AlGaN multiple quantum wells (MQWs)[4]; the other is the demonstration of picosecond (1.2 ps) response at the communication wavelength (1.55 μm) in InGaAs/AlAsSb MQWs.[5]

The growth of GaN/AlGaN MQW wafers, which consisted of four sets of 50 $Al_{0.65}Ga_{0.35}N$ (1.8 nm)/GaN (3.8 nm) QWs separated by GaN intermediate layers, was done on sapphire substrates by use of atmospheric pressure metal-organic chemical vapor deposition.[4] A one-color pump-probe measurement was carried out with a 120-fs pulse generated by an optical parametric amplifier system in a Brewster-angle optics configuration as shown in the inset of Fig. 1(a). A correlation trace of the absorption modulation measured at the 4.5-μm wavelength indicates an extremely fast response (greater than 150 fs), as shown in Fig. 1(a). We believe that this is the record fastest response time ever reported for ISB-T. It is also our belief that this is a result of a significant amount of energy as well as a high scattering rate of longitudinal optical phonons in this material system with high ionicity.

A wafer that consists of 60 periods of $In_{0.53}Ga_{0.47}As$ (2.0 nm)/$AlAs_{0.56}Sb_{0.44}$ (10 nm) QWs lattice matched to InP substrates was grown by molecular beam epitaxy.[5] The absorption spectrum showed a fairly broad peak that extends from 1.5 to 2.5 μm with a center wavelength at 1.95 μm. A two-color pump-probe measurement was performed with 140-fs optical parametric amplifier pulses together with induced white-light pulses. A response trace monitored for the ISB pump at 1.55 μm and the interband (IB) absorption probe at 1.08 μm is shown in Fig. 1(b). A monitored absorption modulation indicates a pulse half-width as short as 1.2 ps, confirming for the first time, to the best of our knowledge, the ultrafast relaxation of ISB-T at communication wavelengths.

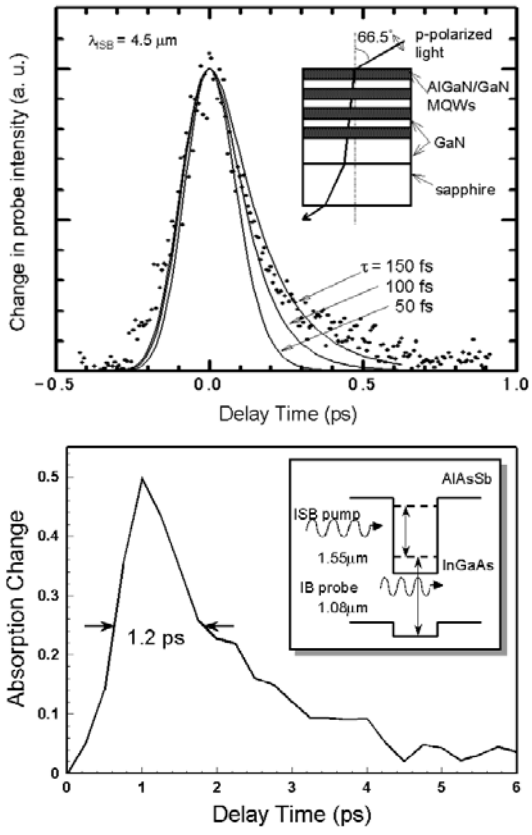

Ultrafast All-Optical Switching Figure 1. (a) Transient response of the ISB-T change caused by the ISB excitation pulse at 4.5 μm in GaN/AlGaN MQWs. The solid curves represent the calculations assuming a two-level system and Gaussian pulses. (b) Transient response of the interband absorption change (monitored at 1.08 μm) caused by ISB excitation with a 1.55-μm pump pulse in InGaAs/AlAsSb MQWs.

Both experimental results have demonstrated promising features of ISB-T as a novel principle of ultrafast, high-repetition all-optical switches unlimited by the carrier recombination lifetime.

Acknowledgments

This research was performed under management of the Femtosecond Technology Research Association (FESTA) supported by the New Energy and Industrial Technology Development Organization (NEDO), and was partly supported by a grant-in-aid for scientific research from the Ministry of Education, Science, Sports, and Culture.

References

1. J. Faist, F. Capasso, D. L. Sivco, C. Sirtori, A. L. Hutchinson, and A. Y. Cho, "Quantum cascade laser," Science **264**, 553-5 (1994).
2. T. Asano, S. Noda, and K. Tomoda, "Pump and probe measurement of intersubband relaxation time in short-wavelength intersubband transition," Appl. Phys. Lett. **74**, 1418-20 (1999).
3. T. Kamiya, F. Saito, O. Wada, and H. Yajima, eds., Femtosecond Technology: From Basic Research to Application Prospects (Springer-Verlag, Berlin, 1999).
4. N. Iizuka, Appl. Phys. Lett. **77**, 648-50 (2000).
5. H. Yoshida, T. Mozume, A. Neogi, N. Georgiev, T. Akiyama, and O. Wada, "Ultrafast all-optical switching using near-infrared intersubband transitions in InGaAs/AlAsSb quantum well structures," in Conference on Lasers and Electro-Optics, Vol. **39** of OSA Trends in Optics and Photonics (Optical Society of America, Washington, D.C., 2000), pp. 357-8.

Terahertz Transceiver

By Qin Chen and X.-C. Zhang

Electro-optic crystals have been widely used in terahertz (THz) time-domain spectroscopy[1] and related imaging applications.[2,3] In a conventional experimental setup of THz time-domain spectroscopy, separate THz transmitters and THz receivers are used for the generation and detection of a THz signal. In certain applications, such as near-field THz measurement at a reflection mode, separate emitters and receivers cannot be used. However, because electro-optic detection is the reverse process of optically rectified generation, the transmitter and the receiver can be the same electro-optic crystal. Therefore, it is feasible to demonstrate a THz transceiver that alternately transmits THz radiation (optical rectification) and receives the returned signal (electro-optic effect), as radar at a microwave frequency. The use of a transceiver has unique advantages for the THz range, remote sensing, and tomographic imaging.[4,5]

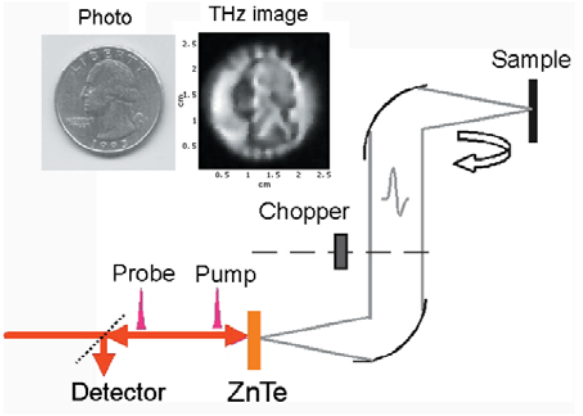

Terahertz Tranceiver Figure 1. Schematic illustration of a THz imaging system with a THz image of a coin that was obtained by use of an electro-optic transceiver.

Fig. 1 shows the experimental setup. The laser is a regenerative amplified Ti:sapphire laser (Coherent Rega 9000). Pulses of 800-nm wavelength and 225-fs duration are produced at a repetition rate of 250 kHz. The electro-optic crystal is a 4.0-mm-thick <110> oriented ZnTe. A pair of synchronized optical pulses (pump and probe) generated by a Michelson interferometer illuminates a <110>-oriented ZnTe crystal. The average power of the pump and probe beam is 100 mW. The first optical pulse generates a THz pulse by optical rectification. The THz pulse is collimated and focused by a pair of parabolic mirrors. A mechanical chopper modulates the THz beam at 450 Hz. The reflected second optical pulse from the second surface of the ZnTe samples the returned THz signal by means of the electro-optic effect with a lock-in amplifier. The polarization directions of the optical pump and probe beam are parallel with each other. Theoretically and experimentally, it has also been demonstrated that the working efficiency of an electro-optic transceiver constructed by a (110) zinc-blende crystal is optimized when the pump beam polarization is 26° counterclockwise from the crystallographic *Z* axis of the crystal. The THz tomographic image of a coin is also shown in Fig. 1.

Compared with the traditional THz tomography setup in standard THz reflection geometry, this imaging system with the electro-optic transceiver is much simpler and easier to align. The measurement of a free-space THz signal that propagates at greater than 10 m is also demonstrated. In addition, the normal incidence of the THz beam on the sample can be maintained, which is crucial for the reflected near-field THz sensing and imaging.

The advantages of the electro-optic transceiver are a broader bandwidth, and the potential for a miniature transceiver. The transceiver crystal can be attached at the end of a polarization-preserved optical fiber with a size of less than 1 mm^3, leading to a truly optical fiber THz transceiver.

Acknowledgment

This research was supported by the U.S. Army Research Office and the U.S. National Science Foundation.

References

1. A. Nahata, A. Weling, and T. Heinz, "A wideband coherent terahertz spectroscopy system using optical rectification and electro-optic sampling," Appl. Phys. Lett. **69**, 2321-3 (1996).
2. X.-C. Zhang and Q. Wu, "New terahertz beams imaging device," Opt. Photon. News **12**, 9-10 (1996).
3. X.-C. Zhang, Q. Wu, and T. D. Hewitt, "Electro-optic imaging of terahertz beams," in Ultrafast Phenomena, Vol. 10 of the Springer Series in Chemical Physics, 54-5 (Springer-Verlag, New York, 1996).
4. M. Tani, Z. Jiang, and X.-C. Zhang, "Photoconductive terahertz transceiver," Electron. Lett. **36**, 804-5 (2000).
5. Q. Chen, Z. Jiang, M. Tani, and X.-C. Zhang, "Electro-optic terahertz transceiver," Electron. Lett. **36**, 1298-9 (2000).

Breaking Metals with Ultrafast Optical Excitation

By Chunlei Guo, George Rodriguez, Ahmed Lobad, and Antoinette J. Taylor

The understanding of structural phase transitions in metals induced by intense laser radiation is important because of its fundamental importance as well as wide applications in materials processing and manufacturing. The dynamics associated with phase transitions, however, constitute a rapidly changing nonequilibrium process that can be resolved only with ultrafast measurements. Recent advances of ultrashort-pulse laser techniques allow for time-resolved measurements of nonequilibrium processes into a regime with femtosecond time resolution.

During the past 20 years, the study of the ultrafast dynamics of perturbative low-intensity laser interaction with metals has been vigorously pursued.[1] Ultrashort pulses, with durations less than or comparable with the excited electron energy-loss lifetime, can heat electrons in a metal to a high temperature while leaving the lattice relatively cool, because the heat capacity of the electrons is much smaller than that of the lattice. This transient two-temperature system will tend to reach equilibrium within a few picoseconds through electron-phonon interaction as well as electron transport out of the excited region. For sufficiently weak incident laser fluence, the excited region of metals will finally reach equilibrium with little disorder. However, if the incident laser fluence is high enough to elevate the final lattice temperature to the melting point, the metal will begin a solid-to-liquid phase transformation. Although structural changes in metals are a vital problem because of the fundamental importance of metal as well as its wide use in materials processing and manufacturing, the understanding of laser-induced melting at a microscopic level is still in its infancy. Further investigation is required for understanding the dynamics associated with melting in metals.

In this investigation we study the dynamics of structural phase transition in aluminum (Al) with ultrafast optical pump-probe measurements.[2] The experiment uses an amplified Ti:sapphire laser system producing more than 700 μJ/pulse in 130-fs pulses with a photon energy of 1.55 eV. In contrast to the ultrafast heating as described above, the structural phase change in Al is predominantly induced by an interband electronic excitation across a pair of parallel bands [Fig. 1(a)]. The dynamics of the structural change following the pump excitation are revealed through monitoring of the time evolution of the dielectric constant with a two-angle probe technique [Fig. 1(b)]. The threshold fluence and the time scale for this structural change in Al are found to be significantly less than the values necessary for ultrafast heat-induced melting. This indicates that the structural phase transition in Al is due to band-structure collapse and lattice instability induced by the strong electronic excitation, which fundamentally differs from the conventional heat-induced melting.

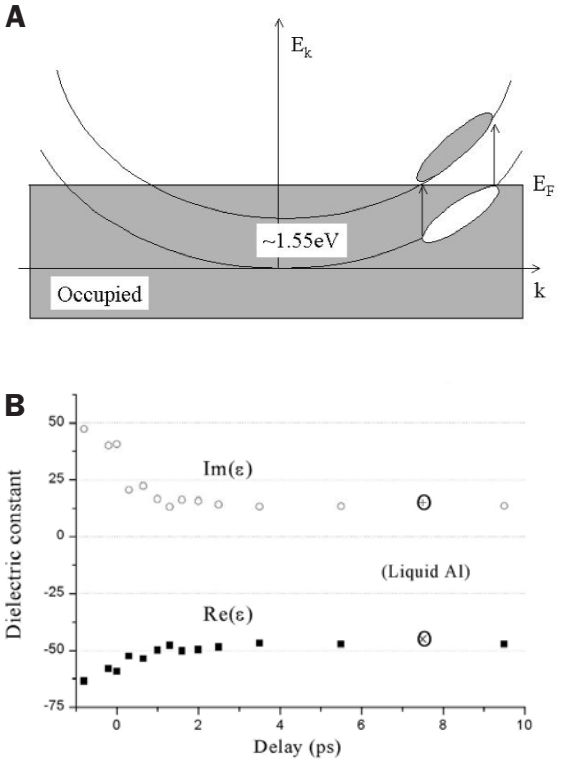

Breaking Metals Figure 1. (A) Parallel band structure of Al, (B) time evolution of the dielectric constant of Al at a fluence above melting threshold indicating the dynamics associated with the melt. The circled = and + in the figure denote the real and the imaginary parts, respectively, of the dielectric constant of liquid Al.

Furthermore, we extended the study of ultrafast dynamics into the conventional heat-induced melting in metals and found pronounced electronic effects in these heating processes.[3,4] The findings presented here provide a more complete understanding of the physical mechanism of metal melting, as well as insights required for designing the optimal procedures for metal processing and manufacturing.

References

1. G. R. Fleming and A. E. Siegman, eds., Ultrafast Phenomena V (Springer-Verlag, New York, 1986), **46**.
2. C. Guo, G. Rodriguez, A. Lobad, and A. J. Taylor, "Structural phase transition of aluminum induced by electronic excitation," Phys. Rev. Lett. **84**, 4493-6 (2000).
3. C. Guo and A. J. Taylor, "Ultrafast electronic disorder in heat-induced structural deformations and phase transitions in metals," Phys. Rev. B **62**, 5382-6 (2000).
4. C. Guo and A. J. Taylor, "Nonthermal component in heat-induced structural deformation and phase transition in gold," Phys. Rev. B **62**, R11921-4 (2000).